Monthly Notices of the ROYAL ASTRONOMICAL SOCIETY

MNRAS **530,** 4560–4577 (2024) https://doi.org/10.1093/mnras/stae1153
Advance Access publication 2024 April 30

Implications on star formation rate indicators from H II regions and diffuse ionized gas in the M101 Group

A. E. Watkins ,[1★] J. C. Mihos,[2] P. Harding[2] and R. Garner, III[3]

[1]*Centre for Astrophysics Research, School of Physics, Astronomy and Mathematics, University of Hertfordshire, College Lane, Hatfield AL10 9AB, UK*
[2]*Department of Astronomy, Case Western Reserve University, 10900 Euclid Avenue, Cleveland, OH 44106, USA*
[3]*George P. and Cynthia W. Mitchell Institute for Fundamental Physics & Astronomy, Texas A&M University, 578 University Drive, College Station, TX 77843, USA*

Accepted 2024 April 29. Received 2024 April 26; in original form 2024 March 26

ABSTRACT

We examine the connection between diffuse ionized gas (DIG), H II regions, and field O and B stars in the nearby spiral M101 and its dwarf companion NGC 5474 using ultra-deep H α narrow-band imaging and archival *GALEX* UV imaging. We find a strong correlation between DIG H α surface brightness and the incident ionizing flux leaked from the nearby H II regions, which we reproduce well using simple CLOUDY simulations. While we also find a strong correlation between H α and co-spatial far-ultraviolet (FUV) surface brightness in DIG, the extinction-corrected integrated UV colours in these regions imply stellar populations too old to produce the necessary ionizing photon flux. Combined, this suggests that H II region leakage, not field OB stars, is the primary source of DIG in the M101 Group. Corroborating this interpretation, we find systematic disagreement between the H α- and FUV-derived star formation rates (SFRs) in the DIG, with $\mathrm{SFR_{H\,\alpha}} < \mathrm{SFR_{FUV}}$ everywhere. Within H II regions, we find a constant SFR ratio of 0.44 to a limit of $\sim 10^{-5}$ $\mathrm{M_{\odot}\,yr^{-1}}$. This result is in tension with other studies of star formation in spiral galaxies, which typically show a declining $\mathrm{SFR_{H\,\alpha}/SFR_{FUV}}$ ratio at low SFR. We reproduce such trends only when considering spatially averaged photometry that mixes H II regions, DIG, and regions lacking H α entirely, suggesting that the declining trends found in other galaxies may result purely from the relative fraction of diffuse flux, leaky compact H II regions, and non-ionizing FUV-emitting stellar populations in different regions within the galaxy.

Key words: ISM: H II regions – ISM: clouds – ISM: evolution – galaxies: star formation – ultraviolet: galaxies.

1 INTRODUCTION

The interstellar medium (ISM) comprises the fuel behind star formation in galaxies. While the stars themselves form from the cold ISM, primarily molecular hydrogen, feedback from this star formation in the form of supernovae, stellar winds, and high-energy photons ensures that much of the ISM exists in a high-temperature, ionized state (McKee & Ostriker 1977; Madsen, Reynolds & Haffner 2006; Haffner et al. 2009). The ionized ISM thus contains a ledger of the ionizing potential of galaxies, a record of which is critical for understanding both the impact of baryonic feedback on galaxy evolution, a necessary constraint on structural cosmological parameters (e.g. Jing et al. 2006; van Daalen et al. 2011; Chisari et al. 2018), and the early evolution of galaxies during the epoch of reionization, an era now increasingly accessible with the advent of *JWST* (e.g. Windhorst et al. 2023).

Of that ionized gas, an important component is morphologically diffuse, and so at a glance appears unassociated with any specific ionization source. Hoyle & Ellis (1963) first proposed the existence of this diffuse ionized gas (DIG) layer in the Milky Way (MW) based on the detection of a free–free absorption signature in the Galactic synchrotron background by Reber & Ellis (1956) and Ellis, Waterworth & Bessell (1962). Reynolds, Roesler & Scherb (1973) eventually detected this layer directly in H α and H β emissions, and later observations with the Wisconsin H α Mapper (Haffner et al. 2003) found that faint H α emission is ubiquitous in the northern sky to a surface brightness of $I_{\mathrm{H}\,\alpha} = 0.1R$ ($\sim 5.7 \times 10^{-19}$ erg s^{-1} cm^{-2} arcsec^{-2}). Gaustad et al. (2001) found similar results in the Southern hemisphere to slightly less sensitivity (0.5*R*). Dettmar (1990) and Rand, Kulkarni & Hester (1990) first identified extragalactic DIG in the edge-on disc galaxy NGC 891, above and below the disc plane, and subsequently, it was found in interarm regions in lower inclination disc and irregular galaxies (Hunter & Gallagher 1990; Walterbos & Braun 1992; Ferguson et al. 1996). It became clear that this DIG (dubbed the warm ionized medium by McKee & Ostriker 1977) is ubiquitous in star-forming galaxies. It occasionally even appears far outside its putative host (e.g. Devine & Bally 1999; Lehnert, Heckman & Weaver 1999; Keel et al. 2012; Watkins et al. 2018).

DIG properties are deeply connected to the structure of the ISM (e.g. Wood et al. 2005; Seon 2009); hence, constraining its ionization source is critical for understanding how such radiation propagates through gaseous media. From the earliest investigations, it was clear that photoionization must be an important such source. For example, the power necessary to ionize DIG is comparable to the total power

★ E-mail: a.emery.watkins@gmail.com

injected by luminous young stars and supernovae, both in the MW (e.g. Reynolds 1990) and elsewhere (e.g. Ferguson et al. 1996). In most DIG, little extra heating beyond photoionization is required to model its observed spectra (Domgorgen & Mathis 1994; Mathis 2000).

The path those ionizing photons take, however, is less straightforward. DIG spectra differ from that of the more compact H II regions, being often relatively elevated in [N II]6549,6584 Å (hereafter, [N II]), [S II]6716,6731 Å (hereafter, [S II]), [O I]6300 Å, and other low-ionization emission lines. Typically, these line strengths increase with decreasing H α surface brightness (e.g. Madsen et al. 2006; Haffner et al. 2009; Hill et al. 2014) and with height above the mid-plane (e.g. Rand 1998; Haffner, Reynolds & Tufte 1999; Otte et al. 2001; Miller & Veilleux 2003; Levy et al. 2019), albeit with wide variability. Photoionization simulations demonstrate that this can be achieved via leakage of ionizing photons from H II regions: because photons with energies near the ionization potential of hydrogen (13.6 eV) are preferentially absorbed in a neutral medium, the ionizing spectrum of the Lyman continuum (LyC) photons that propagate into the diffuse ISM tends to be harder than that found within H II regions (e.g. Wood & Mathis 2004), increasing the kinetic energy of electrons and thus gas temperature. Lines such as [N II] and [S II] are predominantly collisional (Osterbrock & Ferland 2006), thus elevated [N II]/H α and [S II]/H α line ratios imply higher gas temperatures.

Yet [O III]5007 Å, which has a much higher ionizing potential ($\sim$35 eV), sometimes also increases with height beyond what is expected from a hardening LyC spectrum alone (e.g. Rand 1998; Collins & Rand 2001), suggesting some additional ionizing component is necessary to fully explain DIG spectra. Such additional proposals range widely, from post-ABG stars in the stellar halo or thick disc (also known as hot low-mass evolved stars, or HOLMES; e.g. Wood & Mathis 2004; Flores-Fajardo et al. 2011; Rautio et al. 2022), to shock ionization from supernova or active galactic nucleus (AGN) feedback (e.g. Dopita & Sutherland 1995; Simpson et al. 2007; Ho et al. 2014), to magnetic recombination (Raymond 1992; Lazarian et al. 2020). Most likely, many such mechanisms contribute to DIG ionization in different amounts depending on local phenomena, such as the creation of superbubbles (Madsen et al. 2006; Rautio et al. 2022), so the exact fractional contribution of each is still a matter of debate.

Even the photoionization budget is not completely clear, however, as O and B stars outside of H II regions likely contribute to DIG ionization to some extent (possibly nearly 40 per cent; Hoopes & Walterbos 2000; Hoopes, Walterbos & Bothun 2001). Such field O and B stars have been identified in the MW and its satellites (e.g. Gies 1987; Oey, King & Parker 2004; Lamb et al. 2013), and many star-forming galaxies also host substantial extended diffuse far-ultraviolet (FUV) components (Gil de Paz et al. 2005; Thilker et al. 2005, 2007). Some orphan O and B stars are host to their own spherical, ghostly H II regions (e.g. Oey et al. 2013), implying that they do ionize their local ISM and thus can contribute to DIG.

However, it remains unclear where these stars originate, and therefore how their impact might vary as a function of environment. While some may form in the field directly, most others likely formed within clusters and later drifted (‘walk-away’ stars; de Mink et al. 2012; Renzo et al. 2019) or were jettisoned (‘run-away’ stars; Blaauw 1961) to their current locations (e.g. Oey et al. 2004; de Wit et al. 2005; Lamb et al. 2010; Vargas-Salazar et al. 2020). Depending on their velocities, these stars may not stray far from their birth clusters before dying.

If H II region leakage is the primary source of DIG photoionization, one might expect a weak correlation between H α and FUV flux in DIG regions, but a strong correlation between the estimated incident ionizing flux from a galaxy’s H II regions and DIG surface brightness (e.g. Zurita et al. 2002; Seon 2009; Belfiore et al. 2022). DIG would also be predominantly found surrounding H II region complexes, as geometric dilution and neutral ISM absorption would prevent gas ionization elsewhere (save extraplanar DIG, where the plane–parallel approximation is more appropriate and most of the ISM is ionized; e.g. Berkhuijsen, Mitra & Mueller 2006; Flores-Fajardo et al. 2011). If, on the other hand, *in situ* field O and B stars are the primary source, we would see the inverse behaviour in the correlations, and the spatial distribution of DIG would depend on the origins, lifespans, and velocities of the ionizing stars. Contribution from shock ionization or AGN would likely be localized to supernova remnants and galaxy cores, respectively, but would be difficult to isolate without additional diagnostic lines, while HOLMES contribution would be found primarily where old FUV-weak stellar populations dominate, such as the bulge or stellar halo (e.g. Lacerda et al. 2018).

The connection between diffuse H α and diffuse FUV is also mystified somewhat by a well-known discrepancy between H α- and FUV-derived star formation rates (SFRs) in low surface brightness (LSB) regions. Both in the FUV-emitting outer discs of massive galaxies (Goddard, Kennicutt & Ryan-Weber 2010; Byun et al. 2021) and in dwarf and LSB galaxies (e.g. Lee et al. 2009; Meurer et al. 2009; Lee et al. 2016), the ratio between Hα-derived and FUV-derived SFRs is depressed, often to below 50 per cent (but see Bell & Kennicutt 2001). Proposed mechanisms behind this observation in the low-density regime include changes in the stellar initial mass function (e.g. Meurer et al. 2009; Pflamm-Altenburg, Weidner & Kroupa 2009), higher LyC escape fraction in low-mass systems (e.g. Relaño et al. 2012), and less efficient star formation resulting in more sporadic star formation histories (SFHs; e.g. Sullivan et al. 2004; Weisz et al. 2012; Emami et al. 2019). Thus, understanding the origins of DIG is key to the proper utilization of H α emission as an SFR indicator on large spatial scales, and may help illuminate the fundamental physics behind star formation as a whole.

To help provide more constraints on the ionization sources of DIG, we explore the diffuse H α and FUV emission in the M101 Group, a local (D = 6.9 Mpc; Matheson et al. 2012) loose association of galaxies. The group is rather sparse, containing only the massive ($\log(\mathcal{M}_*) = 10.6$; Muñoz-Mateos et al. 2015) face-on spiral M101 (NGC 5457), its lower mass ($\log(\mathcal{M}_*) = 9.1$; Muñoz-Mateos et al. 2015) companion NGC 5474, the irregular star-forming dwarf NGC 5477, and a handful of much fainter satellite candidates, most only recently identified (Müller et al. 2017). Indeed, a recent survey using the *Hubble Space Telescope* found that M101’s satellite population is very sparse, with roughly half the number of low-mass companions as the MW to a limit of $M_V = -7.7$ (Bennet et al. 2020). However, this low group mass, and consequent low velocity dispersion, should allow for more impactful tidal interactions between the group members (Negroponte & White 1983). Integrated light (Mihos et al. 2013) and resolved stellar (Mihos et al. 2018) photometry of M101’s outer disc has illustrated the impact of this on the star formation history (SFH): a burst of star formation which peaked 300–400 Myr ago in M101’s outer disc. Follow-up simulations demonstrate that the most massive companion, NGC 5474, is the most likely culprit (Linden & Mihos 2022).

The group’s well-characterized SFH thus makes it a useful target for studying the origins of the DIG, as it allows one to marginalize SFH as a possible parameter when interpreting H α/FUV SFR ratios. We thus explore the relationship between H II region emission and the DIG surface brightness, as well as that between FUV and H α emission in the DIG, within the M101 group’s most massive members, using archival GaLaxy Evolution EXplorer (*GALEX*; Martin et al. 2005) ultraviolet imaging and our own ultra-deep H α narrow-band imaging done with the Burrell Schmidt Telescope. We give a brief summary of our observations and archival data in Section 2 and Table 1. We describe our methodology behind photometry of DIG and H II regions in Section 3, focusing on measurement and corrections to systematics such as extinction. We present scaling relations derived from our systematics-corrected H α and FUV measurements in Section 4. We discuss these results in Section 5, and finally provide a full summary in Section 6.

2 OBSERVATIONS SUMMARY

We use imaging data from two different observatories for our study. First, we use broad-band and narrow-band images of M101 and NGC 5474 taken with the Burrell Schmidt Telescope (BST) at Kitt Peak National Observatory, a 0.6/0.9m telescope optimized for LSB imaging. Broad-band observations were taken in April of 2009 and April of 2010, in a modified Johnson *B*-band filter (∼200 Å bluer than standard) and in Washington *M*, respectively (Mihos et al. 2013). This broad-band imaging is calibrated directly to Johnson *B* and *V* magnitudes using stars in the field surrounding M101; the details of the photometric calibration can be found in Mihos et al. (2013). Narrow-band observations were taken in April through June of 2014 (H α; Watkins et al. 2017) and March through May of 2018 (H β; Garner et al. 2021), using custom ∼100 Å-wide filters for both on- and off-band observations. In addition, we used archival *GALEX* FUV and near-ultraviolet (NUV) imaging. For M101, we used the deep imaging from the guest investigator programme published in Leroy et al. (2008), and for NGC 5474, we used the imaging from the Nearby Galaxies Atlas (NGA; Gil de Paz et al. 2007) programme.

We summarize the observations in Table 1, including survey, photometric band, resolution on the image coadds, total integration times on-target, and pixel-to-pixel root-mean-square (RMS) uncertainty in the background (in physical flux units). Details of the observation and data reduction strategies used for each set of observations can be found in the associated references (column 9). The BST and *GALEX* pixel scales are 1.45 and 1.5 arcsec pixel^{-1}, respectively.

The RMS uncertainty for the H α difference image is 7.97×10^{-18} erg s^{-1} cm^{-2}, slightly lower than in either narrow-band image individually. This is because much of the background uncertainty in low-resolution imaging comes from unresolved sources, many of which subtract out when creating the difference image.

3 METHODS

We present here our procedure for identifying, measuring the fluxes of, and applying photometric corrections to both H II regions and DIG. We required photometry of both diffuse emission and the more compact H II regions first to separate the two components, and second to assess the impacts of both H II region leakage and field O and B stars on DIG properties.

Our initial catalogue of H II region candidate sources is also likely a mix of true H II regions and interlopers. Thus, we first apply physical corrections to all H II region candidate source photometry, then make interloper cuts based on these physically corrected parameters.

3.1 Detection

We identified both candidate H II regions and DIG regions with the software Sourcerer (formerly, MTObjects; Teeninga et al. 2013, 2016; Haigh et al. 2021). Briefly, Sourcerer performs object detection and segmentation using a max tree algorithm (Salembier, Oliveras & Garrido 1998), which identifies local maxima in an image's flux distribution as leaves of a tree, and nodes as increasingly large connected regions of the image (with the root represented by the entire image). Only those local maxima and connected nodes determined to be statistically significant against the local background are designated as detections, assuming the background has normally distributed noise. Being based on local flux hierarchy, the segmentation Sourcerer performs makes it ideal for identifying embedded point sources, while being simultaneously sensitive to extremely LSB contiguous emission. We ran the software on images cropped around each galaxy separately to ensure the background noise characteristics were not influenced by the variation in exposure counts in different parts of the coadd.

Without access to spectra of most of M101, particularly in its faint outskirts, disentangling DIG and H II region flux can be an ambiguous task. To simplify the process, in both galaxies we chose to label the point-like sources visible in our BST H α difference image as H II region candidates and all other significant H α emission as DIG. This is, to some extent, justified by our images' low resolution. At M101's 6.9 Mpc distance, 1 arcsec corresponds to ∼33 pc, while the distribution of extragalactic H II region radii published by Congiu et al. (2023) shows a peak at roughly ∼90 pc. Our H α narrow-band imaging has a full width at half-maximum (FWHM) ∼ 2 arcsec (Table 1), or 67 pc. Therefore, typical H II regions are barely resolved in our BST imaging, and are unresolved in FUV imaging given that instrument's much larger PSF (FWHM ∼ 4 arcsec).

Even so, our decision to isolate point-like sources defines H II regions as only the most compact and brightest parts of the ionized clouds, likely centred on young star clusters. We recognize this definition differs from that used in many other extragalactic studies (e.g. Thilker, Braun & Walterbos 2000; Erroz-Ferrer et al. 2019; Garner et al. 2021). We consider its impact throughout our analysis.

While the software does segment images using a top-down approach, segmented regions containing point-like sources still typically contain flux from neighbouring diffuse pixels, and so are typically asymmetric. To identify the centres of the point-like sources in each segmented region, we used either the coordinate of each region's brightest pixel, for regions with average surface brightness three times the RMS of the background local to each galaxy, or we used the flux-weighted centroid of the whole region, for sources fainter than this limit, to avoid noise peaks influencing the choice of central coordinate in LSB regions. We show the coordinates of the point-like sources this method identified in the central regions of M101 in Fig. 1, overlaid on our H α difference image.

To separate DIG from H II regions, we applied adaptive masks to each point-like source within the Sourcerer segmentation map. For each source, we scaled the FUV PSF curve of growth to the source's total FUV flux to determine the radius at which the PSF surface brightness dropped a factor of five below our measured FUV limiting surface brightness (for M101 and NGC 5474: $\sim 8.5 \times 10^{-20}$ and 1.2×10^{-19} erg s^{-1} cm^{-2} Å^{-1}, respectively, 1σ on 100 arcsec × 100 arcsec scales). We limited the mask radii between 2 pixel $\leq R \leq$ 10 pixel to avoid over- or under-masking; 10 pixel contains >95 per cent of the total FUV PSF flux, hence even for extremely bright sources this aperture limit suggests only a maximum ∼5 per cent flux contamination for DIG pixels directly adjacent.

We initially assigned every unmasked pixel detected by Sourcerer as DIG. However, even in the native resolution difference image, Sourcerer often identified correlated noise in the background as significant detections, leading to prominent background contamination

Table 1. Table of imaging data used. The columns are 1 – name of survey or instrument from which data is taken; 2 – galaxy covered by survey data given by 1; 3 – photometric band; 4 – effective wavelength of photometric band; 5 – width of photometric band; 6 – PSF FWHM of image coadds; 7 – total integration time on target galaxy; 8 – background root-mean-square uncertainty (erg s^{-1} cm^{-2} Å^{-1} for broad-band, erg s^{-1} cm^{-2} for narrow-band); 9 – reference paper for observations.

Survey (1)	Galaxy (2)	Band (3)	λ_{cen} (4)	$\Delta\lambda$ (5)	FWHM (6)	t_{exp} (7)	RMS (8)	Reference (9)
BST$_{2009}$	Both	*B*	4107 Å	1067 Å	2.5 arcsec	59 × 1200 s	5.40×10^{-20}	Mihos et al. (2013)
BST$_{2010}$	Both	*M*	5088 Å	1207 Å	2.2 arcsec	60 × 900 s	3.25×10^{-20}	Mihos et al. (2013)
BST$_{2014}$	Both	H α-on	6590 Å	101 Å	2 arcsec	71 × 1200 s	9.97×10^{-18}	Watkins, Mihos & Harding (2017)
BST$_{2014}$	Both	H α-off	6726 Å	104 Å	2 arcsec	71 × 1200 s	9.53×10^{-18}	Watkins et al. (2017)
BST$_{2018}$	Both	H β-on	4875 Å	82 Å	2.3 arcsec	59 × 1200 s	6.72×10^{-18}	Garner et al. (2021)
BST$_{2018}$	Both	H β-off	4757 Å	81 Å	2.3 arcsec	55 × 1200 s	6.80×10^{-18}	Garner et al. (2021)
GALEX GI3_050 008	M101	FUV	1530 Å	265 Å	4.2 arcsec	13293.4 s	2.20×10^{-19}	Leroy et al. (2008)
GALEX GI3_050 008	M101	NUV	2303 Å	768 Å	4.9 arcsec	13293.4 s	9.87×10^{-20}	Leroy et al. (2008)
GALEX NGA	NGC 5474	FUV	1530 Å	265 Å	4.2 arcsec	1610 s	1.04×10^{-18}	Gil de Paz et al. (2007)
GALEX NGA	NGC 5474	NUV	2303 Å	768 Å	4.9 arcsec	1610 s	2.99×10^{-19}	Gil de Paz et al. (2007)

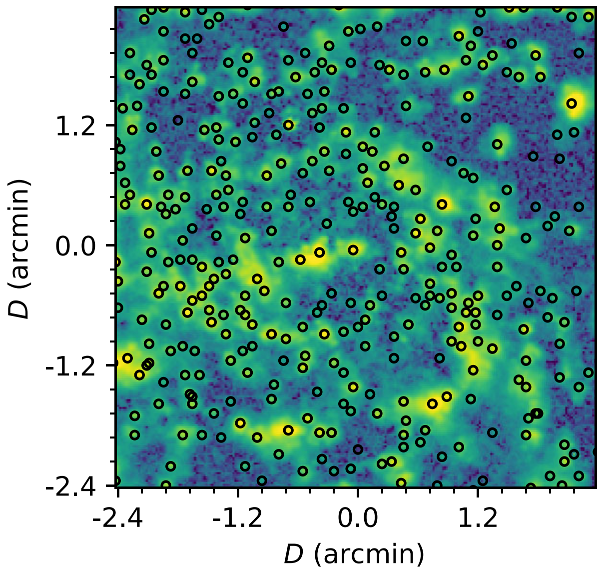

Figure 1. Demonstrating results of our point-like source identification algorithm for the central regions of M101. Black circles are centred on the sources identified by re-centring the segmentation map produced by Sourcerer (see the text), overlaid on a logarithmically scaled image of the BST H α difference image on which we performed the segmentation. Axis labels are distance from the centre of M101 in arcminutes. At M101's distance, $1' \sim 2$ kpc.

in our DIG map. Given our small galaxy sample, we opted simply to erase by-hand all Sourcerer detections at large radius with small size. Comparing scaling relations measured using the initial and cleaned DIG maps shows that our by-hand cleaning removed only long, LSB tails mostly below each band's noise limit. We show cleaned DIG maps for both galaxies in Fig. 2. Any pixel in these maps with a non-zero value, we consider a DIG detection.

Defined in this way, 90 per cent of our DIG pixels have surface brightnesses below $\log(\Sigma_{H\alpha}) < 38.3$ erg s^{-1} kpc^{-2}. This is lower than the DIG–H II region separation threshold proposed by Zhang et al. (2017) ($\log(\Sigma_{H\alpha}) < 39$ erg s^{-1} kpc^{-2}), though many of our DIG pixels have surface brightnesses exceeding their threshold. Our choice to define embedded point sources as H II regions is more comparable to the method employed by Thilker et al. (2000), who define DIG–H II region boundaries using the local gradient of the H α surface brightness, albeit ours is more stringent.

3.2 Photometry

To estimate the impact of H II region flux leakage on surrounding DIG, we required H II region flux estimates free of DIG contamination, and of contamination from neighbouring point-like sources. We thus measured fluxes of each point-like source by masking all neighbouring sources, doing 2 pixel radius aperture photometry of each target (to avoid source crowding; see Fig. 1), then applying background and aperture corrections to estimate total H II region fluxes. We find that, with aperture corrections applied, 3 pixel aperture fluxes are consistent with 2 pixel aperture fluxes to within $\log(F_\lambda) \pm 0.1$ in all photometric bands; hence, our choice of aperture has no impact on the correlations we examine throughout this paper.

We measured local backgrounds as the sigma-clipped median fluxes of unmasked pixels within ring apertures centred on each source, with inner radii of 10 pixel and widths of 2 pixel (chosen to lie beyond the PSF 95 per cent flux radius in all photometric bands). Subtracting these local backgrounds corrects both for DIG contamination and for line absorption from any underlying stellar population (see Garner et al. 2022). We used the aperture corrections published by Morrissey et al. (2007) for *GALEX* bands, and for the BST, we derived our own from our coadds, by stacking and normalizing point sources with signal-to-noise ratios >100 external to all resolved galaxies in the field. We applied aperture corrections only to background-corrected fluxes to derive total fluxes for each source.

DIG photometry required measurements from both the diffuse H α and diffuse FUV emission, to compare DIG and field O and B star populations. This comparison required the H α and FUV images to have the same pixel scale and resolution. Thus, to ensure our DIG segmentation maps matched between photometric bands, we first reprojected our H α on- and off-band images to the *GALEX* pixel scale (a tiny change, from 1.45 arcsec pixel^{-1} to 1.5 arcsec pixel^{-1}) using the ASTROPY-affiliated package REPROJECT (v0.8 – specifically, REPROJECT_ADAPTIVE, which we found best preserved both flux and surface brightness per pixel; Astropy Collaboration et al. 2022). We then convolved each narrow-band image with a normalized Gaussian kernel with $\sigma^2 = \sigma^2_{FUV} - \sigma^2_\lambda$, where σ_λ refers to the standard deviation of our H α on- and off-band averaged coadd

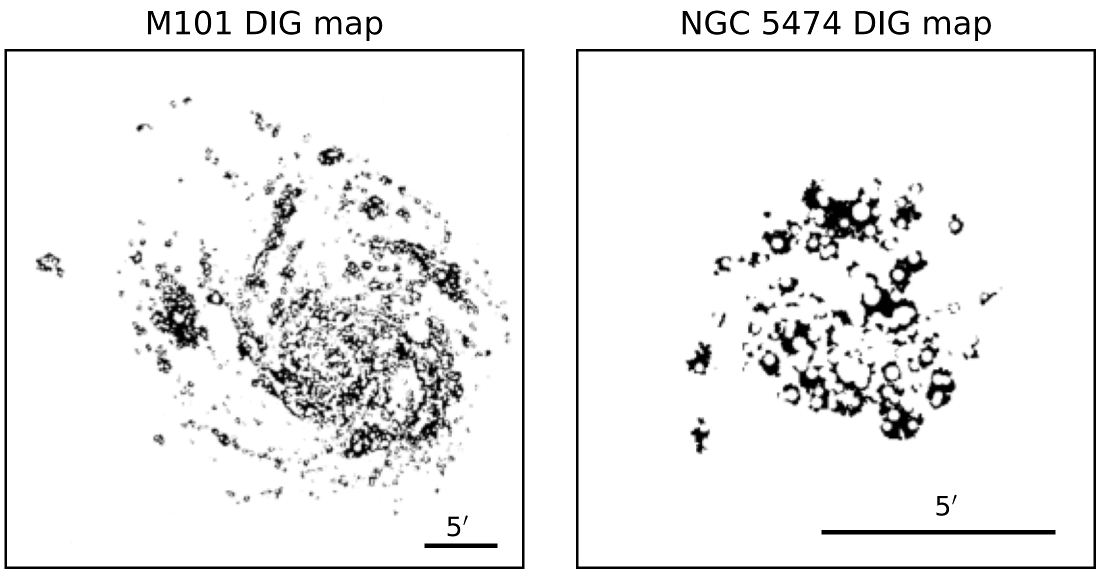

Figure 2. Pixel-to-pixel maps of DIG in M101 (left) and NGC 5474 (right). All non-zero valued (black) pixels we consider DIG. White pixels here are either masked sources or background. We cleaned both maps by-hand of likely spurious detections, meaning those in the outskirts of either galaxy with patchy morphology and small angular size. Black lines show 5 arcmin scale bars. North is up and east is to the left in both panels.

PSFs. Differencing these convolved images resulted in reprojected difference images for each galaxy.

We generated final-generation DIG segmentation maps (Fig. 2) from these reprojected difference images (converted roughly to analogue-to-digital units using the on- and off-band photometric zero-points). We measured DIG fluxes pixel-to-pixel using these maps.

3.3 Photometric corrections

Converting from raw to intrinsic fluxes required correcting for both extinction and for line contamination ([N II] and [S II]) in our narrow-band filters. We describe how we estimated these corrections for both H II regions and DIG in this section.

3.3.1 *H II region corrections*

We first corrected all measured H II region fluxes in all photometric bands for foreground MW extinction. We derived extinction values A_λ in all of our photometric bands using the ASTROPY-affiliated code DUST_EXTINCTION (v1.2; Astropy Collaboration et al. 2022), selecting values of A_λ/A_V from the average MW extinction curve from Gordon, Cartledge & Clayton (2009) and assuming $A_V = 0.023$ (Schlafly & Finkbeiner 2011).

To derive extinction internal to H II regions in both galaxies, we used the Balmer decrement measured from our H α and H β narrow-band images, assuming a theoretical value of $F_{\mathrm{H}\,\alpha}/F_{\mathrm{H}\,\beta} = 2.86$.[1] We first corrected all H β fluxes for internal stellar absorption following Garner et al. (2022), by subtracting from each value 5 Å EW of absorption. This is the average absorption EW for H II regions based on observed and model literature values (González Delgado, Leitherer & Heckman 1999; Gavazzi et al. 2004; Moustakas & Kennicutt 2006). Absorption in H α within H II regions is typically negligible, and our local background subtraction removed any absorption from underlying older stellar populations within the galaxies.

Fig. 3 shows the A_{FUV} gradient for H II regions in both galaxies. The region-to-region dispersion in measured Balmer decrements was quite high ($\sigma_{A_V} > 0.6$ mag at any given radius within M101). Some of this likely arises due to intrinsic variability in dust content and geometry among H II regions; our lack of image resolution thus makes extinction measurements on any individual H II region highly uncertain, even for bright regions with low photometric uncertainty. Hence, for simplicity, we chose to apply global corrections as a function of radius, using linear fits between A_λ and radius for both M101 and NGC 5474, ignoring all regions with $1 < F_{\mathrm{H}\,\alpha}/F_{\mathrm{H}\,\beta} < 8$ (see Garner et al. 2021). In M101, we found that extinction values flattened to $A_V \sim 0.4 \pm 0.9$ (roughly $A_{\mathrm{FUV}} \sim 1$; Fig. 3) beyond ∼300 arcsec (∼10.8 kpc), hence applied a constant extinction correction to all regions found beyond that radius by extrapolating from the last best-fitting point interior to it. NGC 5474 shows no clear radial gradient. Red dashed lines in Fig. 3 show our best-fitting extinction curves for both galaxies.

Our filter placement for the H α narrow-band imaging also included stellar continuum, H α, and [N II] emission in the on-band, and stellar continuum and [S II] emission in the off-band. We thus needed to estimate and correct for both of these emission lines in all derived H α fluxes.

We made these corrections for H II regions in the manner described by Garner et al. (2022), assuming a constant value of [S II]/H $\alpha = 0.2$ and the radial [N II]/[S II] relation given by their equation (2), derived from [N II] and [S II] flux values in M101 published by Croxall et al. (2016). In NGC 5474, again following Garner et al. (2022), we simply applied the average line correction factor for all H II regions within M101 (∼0.95).

[1] Congiu et al. (2023) recommend a theoretical value of $F_{\mathrm{H}\,\alpha}/F_{\mathrm{H}\,\beta} = 3.03$ for DIG-corrected H II region Balmer decrements in star-forming galaxies, but the intrinsic dispersion among measured Balmer decrements in our regions is high enough that the use of this value produced no noticeable change to the extinction gradients we derived in either galaxy.

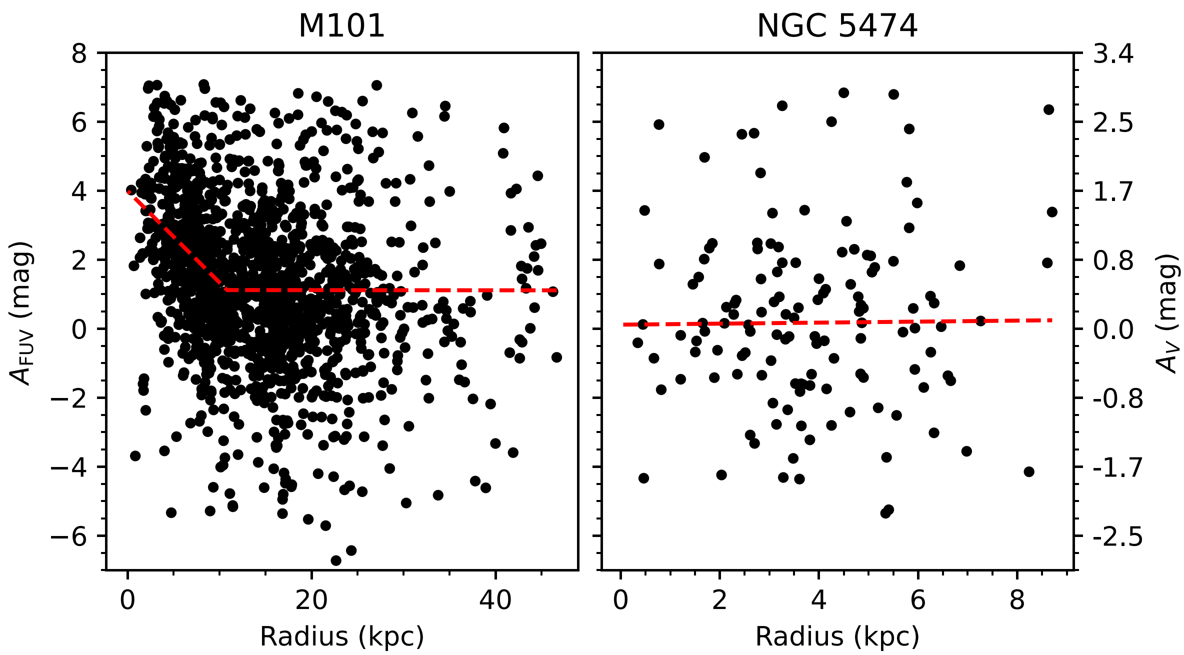

Figure 3. Demonstrating behaviour of extinction internal to H II regions in both galaxies. Each panel shows the distribution of A_{FUV} as a function of radius, as derived from Balmer decrements. The red dashed lines show the best-fitting radial relation in each galaxy. In M101, the gradient flattens beyond ∼11 kpc, hence we assume a constant extinction beyond that radius, extrapolated from the last best-fitting point in the inner relation. NGC 5474 shows no radial extinction gradient and overall lower extinction than M101. We also use these gradients to correct the DIG flux for extinction, albeit employing a different extinction law.

3.3.2 DIG corrections

DIG represents a different physical system than H II regions. Hence, while we applied the same kinds of corrections to DIG, the forms of some of those corrections necessarily differed. The exception is the MW extinction correction, which we applied in the same manner as for the H II regions.

Internal extinction corrections here were less straight-forward. In DIG-dominated regions, we found significant stellar absorption in H β (and mild absorption in H α) in both target galaxies, which is difficult to correct for without spectra. Thus, we used publicly available data from the MUSE atlas of discs (MAD; Erroz-Ferrer et al. 2019), in combination with the H II region metallicities provided by Croxall et al. (2016), to derive an empirical extinction correction for DIG based on our measured H II region extinction gradients. The MAD data includes, for 38 disc galaxies, line fluxes (including [N II], [S II], and H α), measures of gas-phase metallicity, extinction derived from Balmer decrements, and also maps separating out DIG spaxels from H II region spaxels using the method developed by Blanc et al. (2009).

In all MAD galaxies, the median extinction among both H II regions and DIG is roughly constant with radius (when normalized by the effective radius, though the scatter increases sharply toward the galaxy centres). This results from the complex interplay between extinction, stellar mass surface density, and metallicity (Erroz-Ferrer et al. 2019). The DIG extinction, however, shows similar trends to the H II regions, but on average is lower by $A_V \sim 0.1$. Therefore, we assume the same applies for M101 and NGC 5474, and we use our same radial extinction corrections derived from the H II region Balmer decrements to derive internal extinction in the DIG, but offset by $A_V = -0.1$.

DIG and diffuse FUV emission also arises from sources close to the disc plane and so are attenuated primarily by line-of-sight extra-planar dust. Thus, for DIG and diffuse FUV, we use the stellar attenuation curve for low-inclination star-forming galaxies provided by Battisti, Calzetti & Chary (2017, equation 11, with $0.77 < b/a < 1$ coefficients from Table 1, assuming $R_V = 3.64$, their extrapolated value from Table 2) to derive A_λ, rather than that of Gordon et al. (2009).

Some stellar H α absorption was visible from our H α difference image, albeit mild. Making use of Sourcerer's inability to detect negative-valued pixels, we estimated this by masking all Sourcerer detections in both galaxies, then using radial flux profiles of the unmasked flux to estimate corrections as a function of radius. In M101, the correction in the inner 4 kpc was $\sim 4 \times 10^{-18}$ erg s^{-1} cm^{-2} arcsec^{-2} (∼13 per cent of the median DIG H α surface brightness in the same region), decreasing linearly to zero by ∼540 arcsec radius (∼18 kpc). In NGC 5474, the correction in the inner 0.5 kpc was $\sim 1.6 \times 10^{-17}$ erg s^{-1} cm^{-2} arcsec^{-2} (∼40 per cent the median DIG H α surface brightness in that region), decreasing exponentially to zero by ∼110 arcsec radius (∼3.6 kpc). Hence, corrections in both galaxies were small. However, these are lower limits on the true absorption, as some DIG emission may be present in the regions with negative measured flux.

DIG typically shows enhanced [N II]/H α and [S II]/H α compared to H II regions, hence requires different correction factors for these emission lines. We derived these corrections for DIG by investigating the behavior of these lines within the MAD sample DIG spaxels. The cleanest correlation lies between the [N II]/H α ratio and gas-phase metallicity, as nitrogen is produced alongside oxygen in the CNO cycle. The behavior of [S II] is more complex. Sulfur is produced via α-capture, hence is created mostly in massive stars ($> 25\mathcal{M}_\odot$; Weaver, Zimmerman & Woosley 1978; French 1980), giving its abundance a weaker correlation with metallicity. [S II] emission luminosity specifically is a function of sulfur abundance

Table 2. Fit parameters on all regressions discussed in Section 4. Fits are of the form $y = (\alpha \pm \sigma_\alpha)x + (\beta \pm \sigma_\beta)$, where x and y are $\log_{10}$ of the parameters given in column 1. Uncertainties on the fit parameters are given by the σ columns. The subscripts 'ext' and 'line' refer to systematic uncertainties on the fits induced by extinction corrections and corrections for [N II] and [S II] flux contamination, respectively, while σ with no subscript refers to the uncertainty derived from the covariance matrix of the fit residuals. We denote negligible uncertainties using –. The final two columns provide the quadrature sum of all uncertainties for each fit parameter.

Relation	Galaxy	α	σ_α	β	σ_β	$\sigma_{\alpha,\,\mathrm{ext.}}$	$\sigma_{\beta,\,\mathrm{ext.}}$	$\sigma_{\alpha,\,\mathrm{NII,SII}}$	$\sigma_{\beta,\,\mathrm{NII,SII}}$	$\sigma_{\alpha,\,\mathrm{tot}}$	$\sigma_{\beta,\,\mathrm{tot}}$
F_{FUV} versus $F_{\mathrm{H}\,\alpha}$ (H II)	M101	0.957	0.002	0.136	0.410	0.065	0.867	0.005	0.080	0.065	0.962
I_{FUV} versus $I_{\mathrm{H}\,\alpha}$ (DIG)	M101	1.293	–	5.683	–	0.191	3.140	0.018	0.302	0.192	3.154
Q_{10} versus $I_{\mathrm{H}\,\alpha}$	M101	0.735	–	– 21.576	–	0.000	0.000	–	0.002	–	0.002
F_{FUV} versus $F_{\mathrm{H}\,\alpha}$ (H II)	NGC 5474	1.099	0.046	2.623	11.576	0.146	2.142	0.005	0.115	0.153	11.773
I_{FUV} versus $I_{\mathrm{H}\,\alpha}$ (DIG)	NGC 5474	1.378	–	7.393	0.023	0.616	10.694	0.124	2.185	0.628	10.915
Q_{10} versus $I_{\mathrm{H}\,\alpha}$	NGC 5474	0.992	–	– 23.194	0.002	0.000	0.000	–	0.006	–	0.006

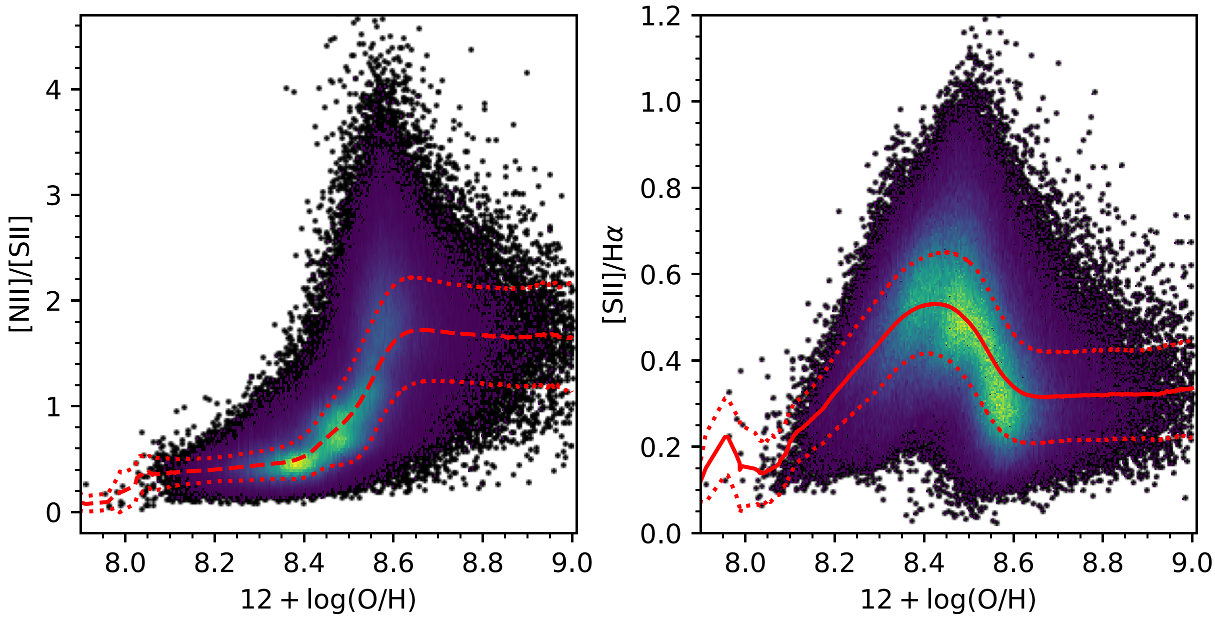

Figure 4. Distribution of [N II]/[S II] and [S II]/H α fluxes in DIG spaxels among MAD sample galaxies (Erroz-Ferrer et al. 2019), as a function of gas-phase metallicity (using the MAD O3N2 calibration). The red dashed lines show the running mean relations, while the red dotted lines show the running standard deviation about those means. We use these relations to correct the DIG H α flux in M101 and NGC 5474 for [N II] and [S II] contamination.

and ionizing radiation hardness (primarily the latter's connection to gas temperature, as [S II] is predominantly collisional; Osterbrock & Ferland 2006). SII's ionization potential is, however, very close to that of the much more abundant He I (23.3 versus 24.6 eV), so hard ionizing radiation preferentially ionizes He I, while slightly softer radiation might preferentially ionize S II into S III, decreasing [S II] emission.

Fig. 4 shows how the [N II]/[S II] ratio and the [S II]/H α ratio vary with gas-phase metallicity (using the [O III] and [N II] empirical calibration, O3N2, from Marino et al. 2013) in the MAD galaxies. The red dashed lines show the running mean relations, while the red dotted lines show the running standard deviations about those means. M101 shows a strong radial metallicity gradient (Croxall et al. 2016; Garner et al. 2022), but most H II regions within M101 have direct-method metallicities between $8.1 < \log(\mathrm{O/H}) < 8.6$. Hence, we derived a radial [N II]/[S II] correction in the DIG using the direct-method radial metallicity gradient provided by equation (10) of Croxall et al. (2016), and we assume a constant value of [S II]/H α = 0.47, the average value among all DIG spaxels in the MAD galaxy sample with metallicities between $8.1 < \log(\mathrm{O/H}) < 8.6$. Using a variable [S II]/H α fraction derived from the median curve in the right panel of Fig. 4 yields a negligible change on our corrected fluxes, hence we opt for the simplicity provided by the constant value.

The median correction we applied for [N II] and [S II] emission in the DIG in M101 is ∼1.3. In NGC 5474, we assume a constant [N II]/[S II] = 0.192, derived from M101's low-metallicity outer disc, and the same value of [S II]/H α = 0.47, for a correction factor of ∼1.6.

3.4 H II region interlopers

To finalize our H II region photometry catalogue, we needed to identify and remove interloping non-H II region sources, typically foreground MW stars and background galaxies. We did this using photometric cuts, demonstrated in Fig. 5.

The left-hand panel shows the $B - V$ colour–magnitude diagram (CMD) of all point-like sources we detected within and surrounding M101, colour-coded by Hα EW in Å. We corrected B, V, and Hα fluxes only for MW extinction in this panel. The CMD is primarily composed of three types of objects: real H II regions,

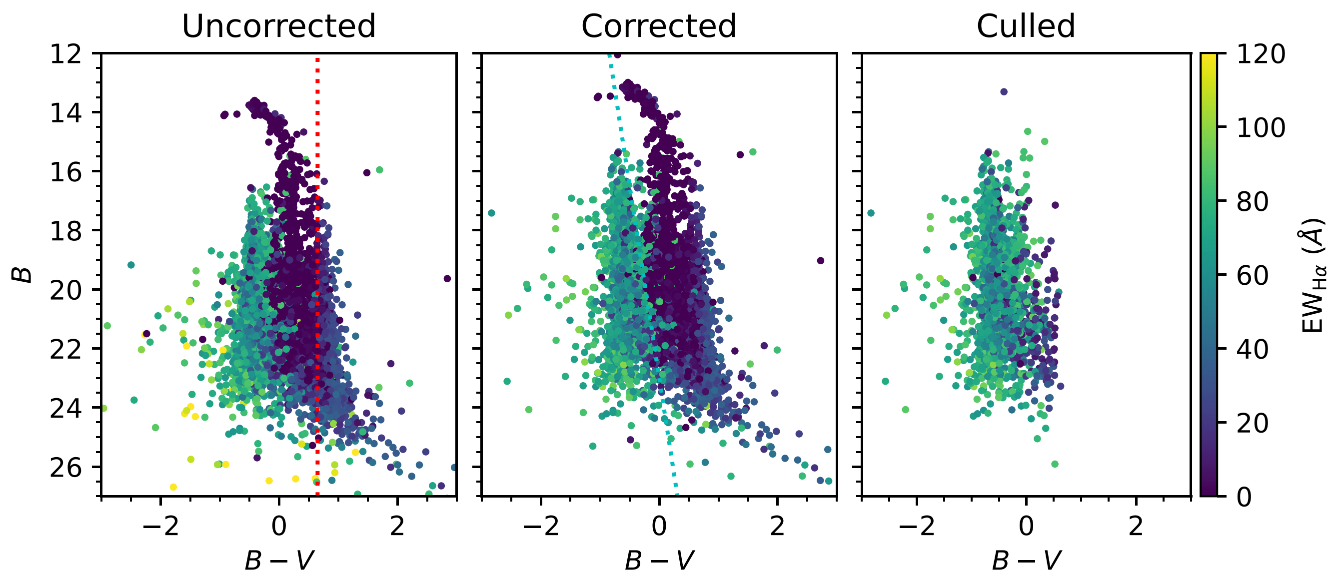

Figure 5. Demonstrating removal of interloping non-H II region sources from our raw point-like source photometry catalogues. The left-hand panel shows the $B - V$ colour–magnitude diagram of all point-like sources detected in M101's vicinity, colour-coded by $EW_{H\,\alpha}$, all corrected only for MW extinction. The central panel shows photometry of the same sources, corrected for MW and internal extinction, with $EW_{H\,\alpha}$ corrected for [N II] and [S II] contamination as well. The right panel shows the sample culled of likely interloping sources. The red dotted line in the left panel shows our initial colour-cut used to reject interloping MW stars ($B - V > 0.65$). The dotted cyan line in the centre panel shows the criteria we chose to identify H II regions using the extinction- and line-contamination-corrected photometry. We accepted as H II regions all sources below the line, as well as any above the line not rejected as MW stars with $EW_{H\,\alpha} > 6$, necessary to preserve the faintest H II regions in both galaxies.

with predominantly blue colours and high $EW_{H\,\alpha}$; interloping MW stars, with a range of colours and predominantly low $EW_{H\,\alpha}$, and interloping background galaxies, with a range of colours and a range of EWs. As noted by Watkins et al. (2017) and Garner et al. (2021), our H α filters are placed such that absorption features in low-temperature MW stars act to depress flux in our off-band filter relative to the continuum in our on-band filter, causing such stars to appear as detections with significant $EW_{H\,\alpha}$ in our difference image.[2] Most such stars are easily identifiable, however, by their red colours; they appear as the column of points with $EW_{H\,\alpha} > 10$ and $B - V > 0.65$. We thus removed anything with uncorrected $B - V > 0.65$ from our H II region catalogue.

The CMD of sources beyond $2 \times R_{25}$ in either galaxy lacked the distribution of points with blue colours ($B - V \lesssim 0.5$) and high $EW_{H\,\alpha}$ ($EW_{H\,\alpha} \gtrsim 40$) seen in the left and central panels of Fig. 5. We thus applied a colour-cut to isolate H II regions from stars, shown by the dotted cyan line in the central panel of Fig. 5, which we make after applying extinction, [N II], and [S II] corrections to all sources. To balance star removal with preservation of faint H II regions, we also excluded all such sources with corrected $EW_{H\,\alpha} < 6$. The final H II region catalogue CMD, corrected for all of the factors described in the preceding sections, is shown in the rightmost panel of Fig. 5. Our final catalogue contains 1954 H II regions in M101 and 161 H II regions in NGC 5474.

To assess the impact of our choice to limit H II region photometry to only point-like emission, we estimated the high-luminosity power-law index of M101's H II region luminosity function. The best-fitting slope above $\log(L_{H\,II}) > 37.5$ erg s^{-1} yields $\alpha = -1.98$, within the uncertainty of ±0.2 published by Kennicutt, Edgar & Hodge (1989) for the same luminosity range. This suggests that isolating flux measurements to only the brightest point-like parts of H II regions is not unreasonable, and produces results consistent with other methods. The largest differences likely arise for low flux objects, below the luminosity function knee.

[2]For example, the single point with $EW_{H\,\alpha} \sim 80$ Å and $B - V \sim 1.5$ is a nearby long-period variable star (Tycho 3852-296-1; Høg et al. 2000; Gaia Collaboration 2022).

4 RESULTS

In the event that most DIG emission arises due to leaked LyC photons from H II regions, we would expect a strong correlation between DIG H α surface brightness (hereafter, $I_{H\,\alpha}$) and the luminosities of nearby H II regions. Likewise, if most DIG emission arises from *in situ* field O and B stars, we would expect a strong correlation between DIG $I_{H\,\alpha}$ and the cospatial FUV surface brightness (I_{FUV}). Hence, in this section, we showcase two correlations: that between DIG $I_{H\alpha}$ and the incident ionizing flux of each DIG pixel's nearest ten H II regions, estimated from their H α luminosities; and that between DIG $I_{H\,\alpha}$ and I_{FUV} of the same regions. For comparison, we also show the relationship between Hα and FUV flux among the point-like H II regions. Where appropriate, we also convert the H α and FUV surface brightnesses and fluxes into SFRs using the same calibrations as Lee et al. (2009) and Byun et al. (2021), derived from Kennicutt (1998) and Kennicutt & Evans (2012). We concentrate on these two scenarios (leakage and field stars) because both M101 and NGC 5474 show prominent, wide-spread star formation. We thus expect the contribution from HOLMES to be relatively small, and we lack the detailed spectroscopy necessary to identify shocked gas emission.

For each fit, we employed the SCIPY.ODR (V.1.10.0) implementation of orthogonal distance regression (ODR; Boggs & Donaldson 1989), weighting the fits on each axis by the combined photometric and calibration uncertainty where applicable. We adopted calibration uncertainties of 10 per cent for both H α and FUV (Morrissey et al.

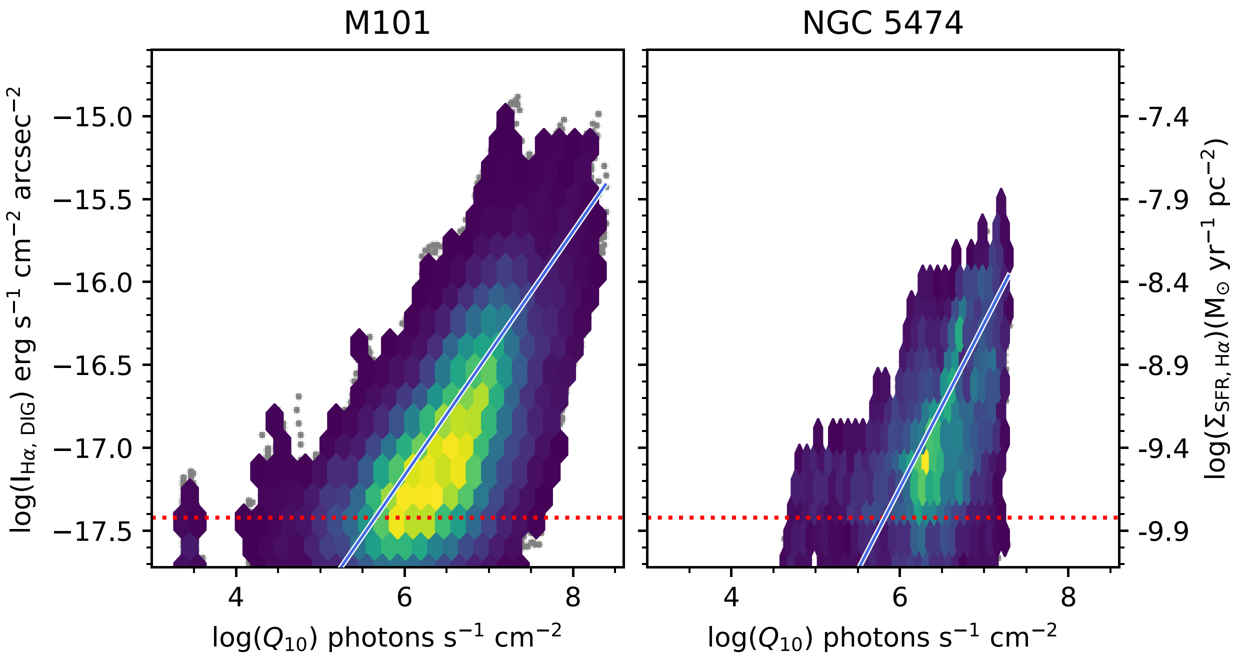

Figure 6. H α surface brightness in the DIG as a function of the number of ionizing photons incident on each DIG pixel from the nearest 10 H II regions, derived from the H α fluxes of said regions, uncorrected for internal extinction. DIG pixels without significant H α flux are excluded here. The colour scale in the 2D hexagon histogram denotes the density of points in each bin, with individual points shown in gray underneath. The blue lines show the best-fitting relations (Table 2). The dotted red line denotes the RMS in the H α image background, which sets our noise limit.

2007; Garner et al. 2022). For H α, the value derives from the combined uncertainty between the on- and off-band zero-points, with a small amount added to consider uncertainty from photometric corrections (Section 3.3). This simply sets a ceiling to the weights; we find that the fits are insensitive to the exact values adopted, within reason.

We provide the best-fitting slopes and intercepts for each relation we discuss in this section in Table 2, including both standard errors derived from the covariance matrix of the regression residuals, and systematic uncertainties from our extinction, [S II], and [N II] contamination corrections. Where the uncertainties are negligible, as in the case of the standard errors when the number of points used in the fit is large (e.g. the $I_{\mathrm{H}\,\alpha}$–I_{FUV} relations, which use tens to hundreds of thousands of points), we do not report them.

We derived the systematic uncertainties using a Monte-Carlo approach, with $N = 100$ iterations per fit. First, we perturbed the best-fitting parameters of the extinction, [N II], and [S II] relations used to derive the corrections (radial for the former, metallicity for the latter) using normal distributions with $\mathcal{N}(0, \sigma_\alpha)$ and $\mathcal{N}(0, \sigma_\beta)$, where σ_α and σ_β are the standard errors on the slopes and intercepts, respectively, of each systematic relation. Additionally, we perturbed the mean [S II]/H α ratio we applied for that correction by the standard deviation of that ratio in each case (H II region and DIG). We then re-derived all relevant fluxes using these perturbed relations, and re-derived each correlation using the same ODR approach as before. We adopted the standard deviation of the $N = 100$ perturbed fit parameters as the systematic uncertainty in each case. We provide total uncertainties on the fit parameters in the last two columns of Table 2, which are the quadrature sum of all uncertainties.

As one additional but important point, we measure the total H α fluxes within M101 and NGC 5474 to be $\log(F_{\mathrm{H}\,\alpha}) = -10.00$ and -11.54 erg s^{-1} cm^{-2}, respectively (as this is merely a side-note, we eschew a formal estimate of uncertainties on these values, but at minimum they are ± 0.05, or $\sim$10 per cent from the flux calibration). These are very similar, within the uncertainties, to the values published by Kennicutt et al. (2008) of -10.23 ± 0.13 and -11.55 ± 0.05, respectively (adjusted for our adopted distance of 6.9 Mpc), in agreement with the conclusions of Lee et al. (2016). Interestingly, the largest discrepancy is with the more massive galaxy, M101, where it is not expected (Lee et al. 2009).

4.1 DIG H α surface brightness versus incident flux from H II regions

To consider the impact of H II region LyC leakage on DIG, Fig. 6 shows the correlation between the $I_{\mathrm{H}\,\alpha}$ of the DIG and the incident ionizing flux from the nearest ten H II regions at each DIG pixel, for both M101 (left) and NGC 5474 (right). We show the best-fitting correlation for each galaxy as solid blue lines. We chose the nearest ten regions because we found the contribution from any regions beyond this to be negligible, and changing the analysis to the nearest nine or eight regions made no substantive change to our results.

We estimated the incident ionizing flux by summing the geometrically diluted H α flux of the nearest ten H II regions incident on each DIG pixel, estimated from the regions' H α luminosities. We converted this total H α flux to an ionizing radiation flux using the relation $L(\mathrm{H}\,\alpha) = 1.37 \times 10^{-12} Q$ (Osterbrock & Ferland 2006), where Q is the ionizing photon rate in units of photons s^{-1}. We denote this incident ionizing flux as Q_{10}, which has units of photons s^{-1} cm^{-2}. We do not correct the H II region luminosities for internal extinction in this step, as we assume that the incident flux at any given DIG pixel is that which escapes from the H II region, not its geometrically diluted intrinsic brightness. As such, systematic uncertainties on these values do not include any contribution from

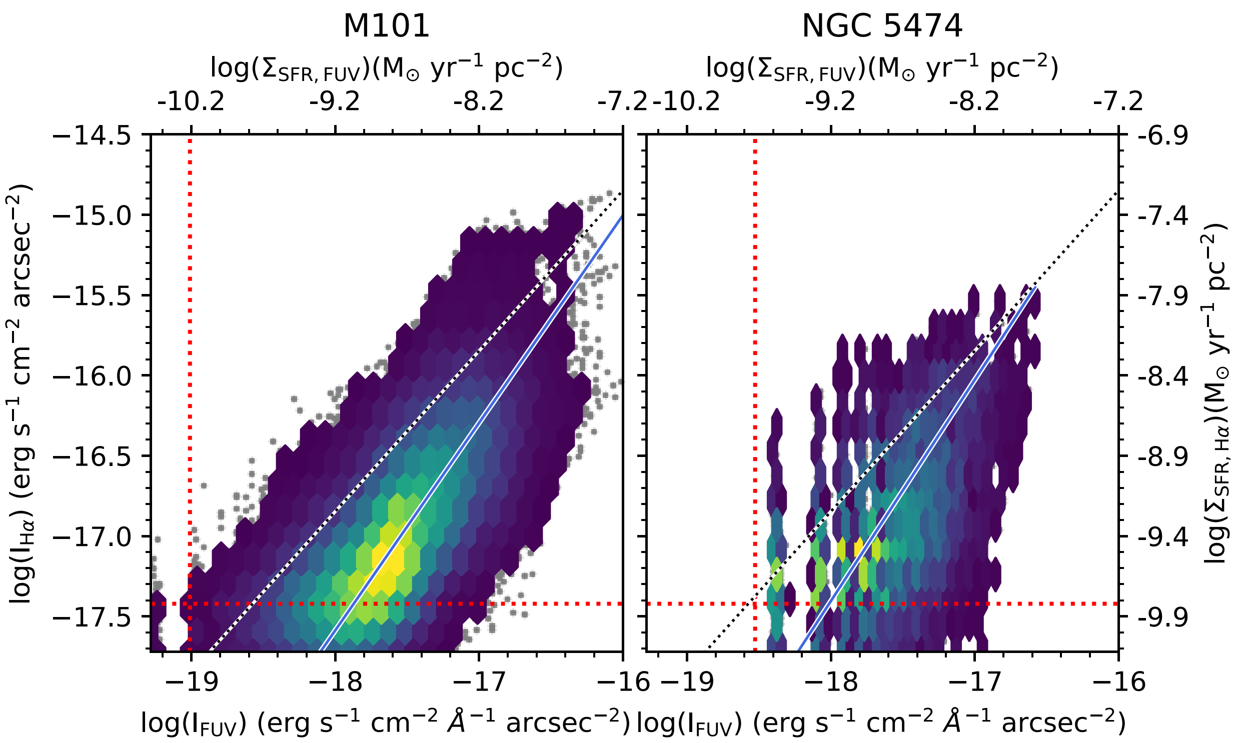

Figure 7. Pixel-to-pixel FUV versus H α surface brightness in the DIG of both galaxies. The plotting schema is the same as 6, but we have included also a vertical red dotted line showing the RMS in the FUV image backgrounds. The top and right axes show surface brightness converted to SFR surface density from either band (FUV at the top and H α at the right). Dotted black lines show the 1:1 relation in SFR.

an extinction correction, although the relations change very little if we do employ extinction-corrected H II region luminosities.

Both galaxies show a strong positive correlation between incident ionizing flux and DIG $I_{\mathrm{H}\,\alpha}$, with slopes between ~0.7–1 (Table 2), implying that leakage from H II regions is an important contributor to the DIG in both galaxies. We are, of course, making some physical assumptions by estimating the incident ionizing flux in this manner. If LyC photons leak from the H II regions, the value of Q we estimate for each H II region from $L_{\mathrm{H}\,\alpha}$ corresponds to the total value of Q minus the fraction which escapes into the ISM. Thus, by assuming that the value of Q we estimate for each H II region is the same as that leaking out to ionize the DIG, we implicitly assume $f_{\mathrm{esc}} = 0.5$. We explore this assumption's validity in Section 5.2, in which we investigate how well our measured relation agrees with estimates from models, and what this implies about the fraction of DIG ionization contributed by this leakage compared to the other potential source we investigate, field O and B stars.

4.2 H α versus FUV

A strong correlation between diffuse H α and the FUV emission in the DIG regions may suggest that field O and B stars contribute heavily to the DIG emission, while a break in such a relation would suggest a transition from one DIG regime (perhaps dominated by H II region leakage) to another. To assess this potential contribution in the M101 Group, we show the correlation between H α and FUV surface brightness and flux for the DIG and H II regions in Figs 7 and 8. As before, we show the best-fitting correlations as solid blue lines. Dotted black lines show the relation where the SFR ratio is unity. Dotted red lines in Fig. 7 designate the RMS in the background, which serves as limiting surface brightnesses in both bands for the pixel-to-pixel photometry.

In the DIG (Fig. 7), we see a correlation with an unbroken slope close to one (~1.3 ± 0.2), with the $\mathrm{SFR}_{\mathrm{H}\,\alpha}/\mathrm{SFR}_{\mathrm{FUV}}$ ratio declining as a function of surface brightness in both bands. This suggests that, while there may be a connection between the diffuse FUV and H α components in these galaxies, it is likely not as straight-forward as direct ionization by field O and B stars. We discuss such stars' possible contribution in Section 5.2.

In the H II regions, the SFR ratio is constant across the full range of flux values. In M101, this ratio is below unity (in linear units, $\mathrm{SFR}_{\mathrm{H}\,\alpha}/\mathrm{SFR}_{\mathrm{FUV}} \sim 0.44$). In NGC 5474 it is consistent with unity, although the fit uncertainty is much higher than for M101. Regardless, this near constant SFR ratio among H II regions provides a seeming contrast to results from past studies (e.g. Lee et al. 2009, 2016; Byun et al. 2021). We discuss the implications of this in Section 5.1.

5 DISCUSSION

5.1 Separation of H II regions and DIG

We showed in Section 4 that the average trend among what we defined as DIG pixels showed depressed $\mathrm{SFR}_{\mathrm{H}\,\alpha}/\mathrm{SFR}_{\mathrm{FUV}}$ universally, declining with $I_{\mathrm{H}\,\alpha}$. We also found that Hα SFRs measured from the point-like objects which we identified as H II regions are about half those predicted by the FUV fluxes at all luminosities. So while the DIG trend seemingly reflects what was discovered in past

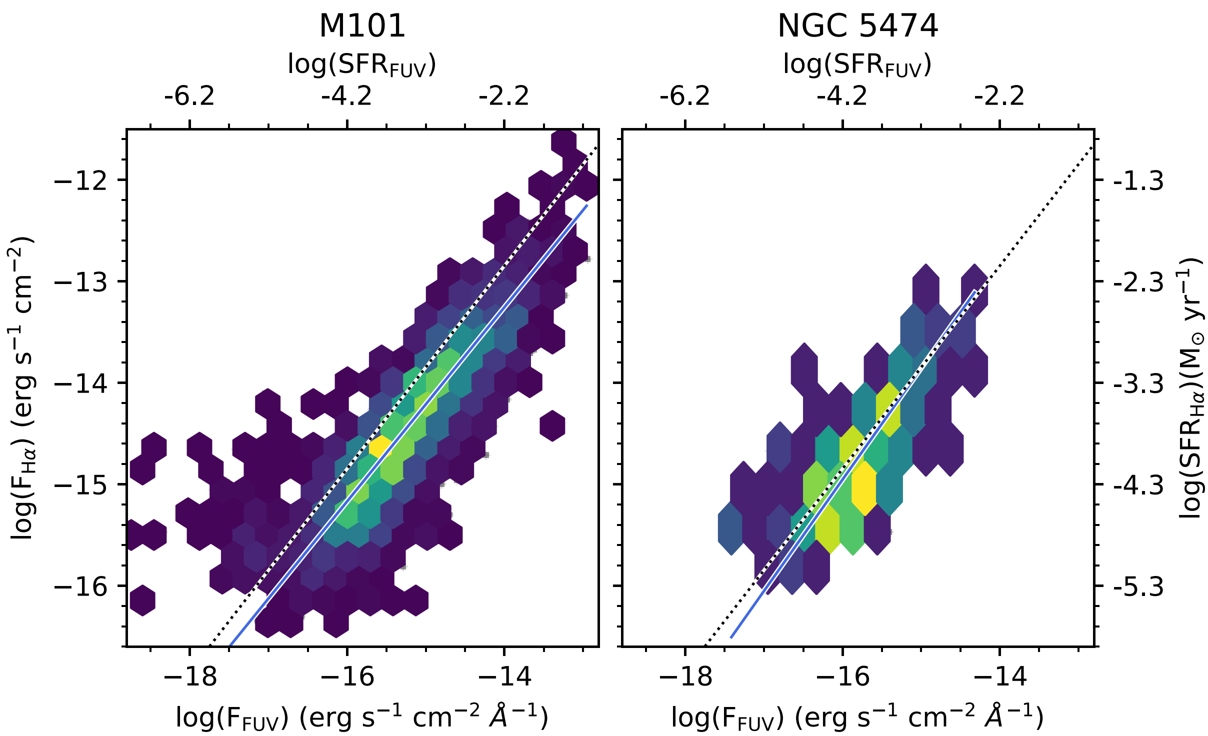

Figure 8. As Fig. 7, but for H II regions. The axis limits differ here, as the luminosities probed are much higher. RMS limits fall outside of the axis limits in this figure.

investigations of this ratio (e.g. Meurer et al. 2009; Lee et al. 2016; Byun et al. 2021), the H II region trend does not, despite that we use the same SFR calibrations as those studies.

Lee et al. (2009) found that the two SFR indicators diverge below $\mathrm{SFR_{H\alpha}} \sim 0.003\mathcal{M}_\odot$ yr^{-1} ($\log(\mathrm{SFR_{H\alpha}}) \sim -2.5$) using integrated SFRs of dwarf galaxies. Byun et al. (2021) later corroborated this finding locally within two spiral galaxies, measuring SFRs within 6 arcsec radius circular apertures (∼300 pc at their targets' distances) positioned on a hexagonal grid. Goddard et al. (2010) also found that H α truncates much more rapidly than FUV in the azimuthally averaged surface brightness profiles of many disc galaxies. Each of these studies thus used photometry of regions with larger spatial scales than our study, with apertures that likely contained both DIG and H II regions.

Part of the discrepancy between our results and these others may thus be methodological, as we measure our fluxes through separation of point-like star-forming regions and diffuse regions. We demonstrate this in Fig. 9, which shows $\log(\mathrm{SFR_{H\,\alpha}}/\mathrm{SFR_{FUV}})$ as a function of $\log(\mathrm{SFR_{H\,\alpha}})$ for three different cases. In the top panel, we measured this ratio using a grid of box apertures across M101, with sizes of 18 arcsec × 18 arcsec (∼600 pc at M101's distance, to mimic Byun et al. 2021), summing all flux (H II region, DIG, and FUV with no H α counterpart) within each box. The bottom two panels show this same trend for our point-like H II region and pixel-to-pixel DIG region samples, measured as described in Section 3. The horizontal black dashed lines show equal SFRs, while the vertical blue dashed lines show $\mathrm{SFR_{H\alpha}} \sim 0.003\mathcal{M}_\odot$ yr^{-1}. The red vertical dashed lines are our limiting Hα surface brightness converted to a per-pixel SFR.

Using these larger box apertures, we do reproduce the trend found by Byun et al. (2021), where only regions with the highest SFRs (near $\mathrm{SFR_{H\alpha}} \sim 0.003\mathcal{M}_\odot$ yr^{-1}) show SFR ratios approaching unity. However, the other two panels provide additional context: when summing both DIG and point-like H II region flux, the trend appears as a kind of convolution of the flat H II region trend and the declining DIG trend.

Fig. 10 also demonstrates this using azimuthally averaged profiles of $\log(\mathrm{SFR_{H\,\alpha}}/\mathrm{SFR_{FUV}})$, shown as a function of disc scale length as measured in the *B* band. Each curve shows the average flux within concentric circular annulus apertures for three different cases: DIG pixels only (purple), H II regions only (green), and all flux (gold; again, including FUV flux with no H α counterpart). While the ratio remains fairly constant in both the DIG and H II region curves (at ∼0.3 and ∼0.5 in linear units, respectively), the azimuthally averaged profile using all flux shows a strong decline in the ratio in M101 and a subtle decline in NGC 5474. Beyond a few scale lengths in either galaxy, the azimuthally averaged H α flux has dropped to nearly zero, hence both profiles truncate.

The decline in the SFR ratio with $\mathrm{SFR_{H\,\alpha}}$ in the M101 Group thus seems to result from a transition from the regime spanned by the point-like H II regions, where the ratio is constant, to the DIG regime, where it declines. The reason for the decline in the DIG regime may result from a change in FUV-emitting stellar populations there compared to the bright young clusters found within the H II regions. Both M101 and NGC 5474 show abundant FUV emission with no H α counterpart, with it being particularly prevalent in M101's outer disc. Indeed, we found that the fraction of pixels in each 18 arcsec × 18 arcsec box used in the top panel of Fig. 9 with significant FUV emission (above the background RMS) but no significant H α emission (below the RMS) shows a strong negative correlation with SFR. Using an alternative DIG map based on the FUV image, we found that around 27 per cent of this H α-less diffuse FUV emission

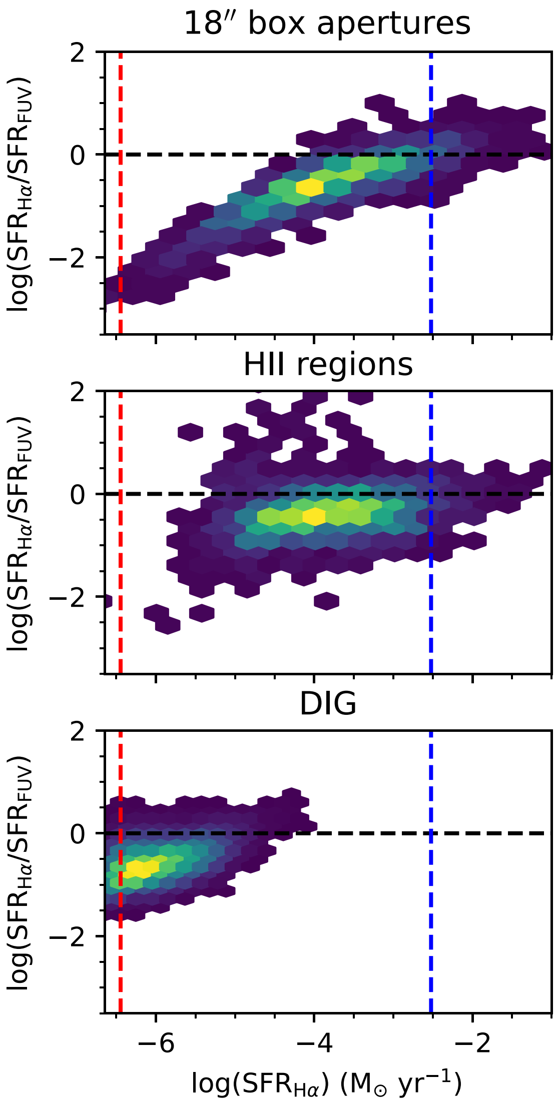

Figure 9. H α- to FUV-derived SFR ratio as a function of H α-derived SFRs measured in different environments. The top panel shows these values measured using a grid of 18 arcsec × 18 arcsec box apertures, summing all flux (i.e. not Hα-selected only) in each box. The central and bottom panels show these values for our point-like source H II region and pixel-to-pixel DIG samples, respectively. The black horizontal line denotes equality in both SFR indicators. The blue vertical line denotes SFR$= 0.003\mathcal{M}_\odot$ yr^{-1}, the value below which Lee et al. (2009) and Byun et al. (2021) found the two SFR indicators to diverge. The red vertical line denotes our limiting Hα surface brightness, converted to SFR.

would have a detectable H α counterpart in our imaging were the ratio $F_{H\alpha}/F_{FUV}$ in the DIG the same as it is in the H II regions. This could occur either if DIG stars are less massive (thus producing fewer LyC photons) than those in the H II regions, or if the DIG environment has a much higher f_{esc}. We explore this in the following section.

5.2 DIG origins in the M101 Group

As demonstrated in Section 4.2, there is a tight, nearly one-to-one correlation between H α and FUV surface brightness in the DIG. This suggests that field O and B stars may contribute a substantial fraction of the power required to ionize it. However, there is no break in the relation, as one might expect in LSB regions where ionization from H II regions has diluted. We thus cannot rule out that the close correlation might arise simply because the two types of emission are tracing the same underlying phenomenon: that both young massive stars and DIG tend not to stray far from H II regions, even if for very different reasons.

For example, Oey et al. (2018) estimated a velocity dispersion of field O and B stars (more massive than spectral type B0.5) in the Small Magellanic Cloud using *Gaia* Data Release 2 (Gaia Collaboration et al. 2018) of ∼40 km s^{-1} in any one direction. If this is comparable in M101, over a 10 Myr timespan (roughly the lifespan of such stars), these would travel ∼400 pc from their natal clusters on average. For comparison, the median distance between all DIG pixels and their nearest neighbour H II regions in M101 is 389 pc, and in NGC 5474 is 358 pc.

DIG thus does not stray much farther from H II regions than typical field O and B stars would if those stars originated within the same regions as the current star formation. DIG also exists primarily in regions with high gas density, where on-going star-formation is more likely. By cross-matching our DIG pixel coordinates with the H I moment zero map of M101 from The H I Nearby Galaxy Survey (THINGS; Walter et al. 2008), we found that the H I emission in DIG pixels shows a fairly steady value of $\log(N_{H\,I}) = 20.67$ cm^{-2} ($\sim 3.4\mathcal{M}_\odot$ pc^{-2}) across either galaxy, fairly typical of star-forming regions in spirals (e.g. Bigiel et al. 2008).

One way in which we can assess the likelihood that these field O and B stars are powering the DIG is by examining the diffuse FUV stellar populations through integrated colour. Fig. 11 shows an FUV−NUV (AB magnitudes) colour map of M101, with white contours outlining the DIG and H II regions. Here, we have corrected both FUV and NUV flux for extinction as described in Section 3.3.

It is clear at a glance that FUV-emitting populations located outside of either DIG or H II regions show systematically redder colours than those located within those regions, and that H II regions themselves show bluer colours than DIG regions. To be more quantitative, the average colour within the white contours is FUV−NUV = 0.31 ± 0.24, compared to FUV−NUV = 0.44 ± 0.25 outside of the contours (including all pixels, inner and outer disc alike), while the H II regions have a mean colour of 0.05 ± 0.27. Most of the scatter in these colours seems to arise from variability in extinction rather than intrinsic variability or photometric uncertainty. We reproduce the distribution of both DIG and H II region colours well using their median colours perturbed by normally distributed extinction corrections with a standard deviation of 0.6 mag, roughly the scatter about our best-fitting extinction gradient in M101.

Using the population synthesis software Code Investigating GALaxy Emission (CIGALE; Burgarella, Buat & Iglesias-Páramo 2005; Noll et al. 2009; Boquien et al. 2019),[3] we found that a colour as red as FUV−NUV = 0.3 is difficult to produce in the presence of a substantial population of young O stars. A population modelled as a recent (25 Myr ago) burst atop a constant SFR (a reasonable model of M101) always maintains colours <0, while a single fading starburst does not reach a colour of 0.3 until ∼150 Myr of age, by which point its ionizing flux is too low by several orders of magnitude to produce even the lowest values of $I_{H\alpha}$ we measure in the DIG. Similarly, a simulation of a fading burst using the galaxy evolution software GALEV (Kotulla et al. 2009) reaches the same colour by ∼400 Myr of age, by which time its ionizing flux is vanishingly small.

[3] https://cigale.lam.fr/

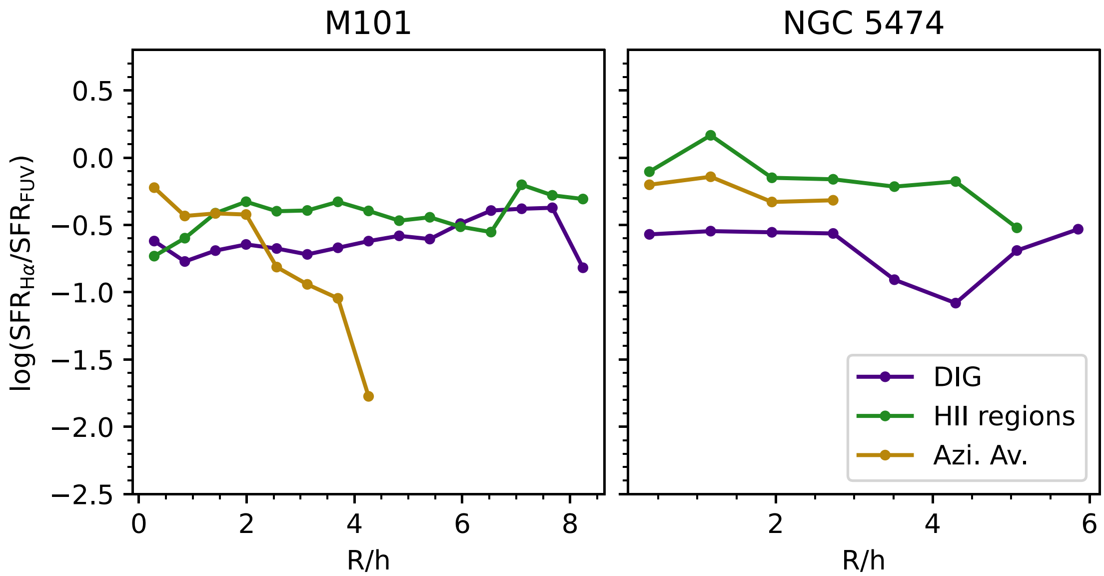

Figure 10. Azimuthally averaged radial profiles of SFR ratio, for three different cases: DIG pixels only (purple), H II regions only (green), and all flux (gold), including FUV emission with no H α counterpart. Gold profiles truncate where background begins to dominate in the H α image. Radii are scaled by each galaxy's *B*-band scale length, which are 4.42 kpc (2.2 arcsec; Mihos et al. 2013) and 1.29 kpc (0.64 arcsec, measured for this work) for M101 and NGC 5474, respectively.

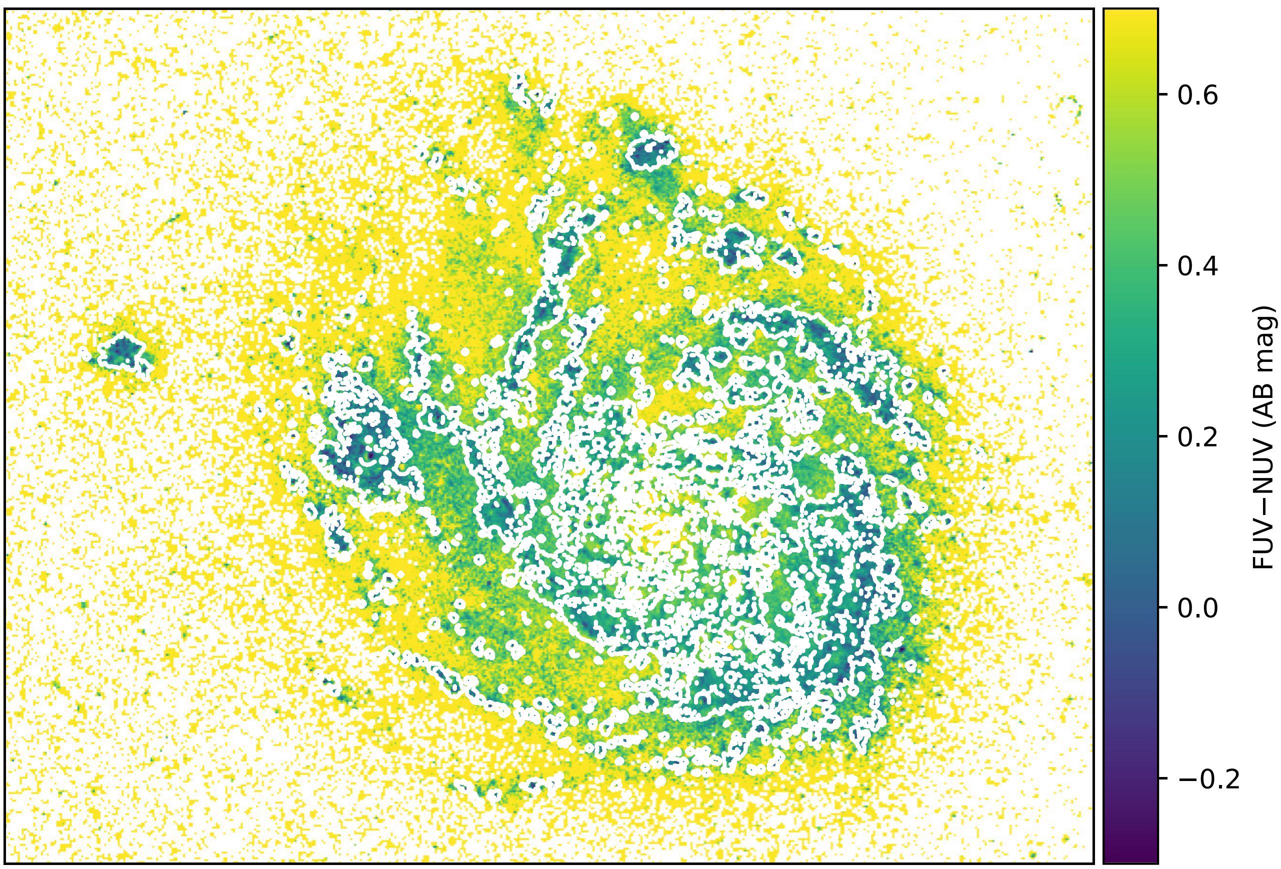

Figure 11. Extinction-correction FUV−NUV colour map of M101, in AB magnitudes. White contours outline the DIG and H II regions.

This therefore suggests that, despite the spatial coincidence between DIG and diffuse FUV near H II regions, the field O and B star contribution to DIG is minimal in the M101 Group, on average. The large-scale diffuse FUV component in both galaxies could well be a remnant of the tidal interaction between M101 and NGC 5474 ~300–400 Myr ago (Mihos et al. 2013, 2018; Linden & Mihos 2022), with the FUV most coincident with the DIG being remnants of dissolved clusters from earlier episodes of star-formation in the spiral arms (likely streamed there after forming within spiral arms; e.g. Crocker et al. 2015; Garner et al. 2024). If the large-scale FUV emitted by these redder stars has a corresponding DIG equivalent, it lies at surface brightnesses below our sensitivity, and hence cannot be constrained using our data.

If field O and B stars contribute little, this diffuse gas must comprise a distinct physical environment from the point-like H II regions. We must therefore consider some alternative sources of ionization. A study by Lacerda et al. (2018) found that in Sc galaxies like M101, the LyC contribution from older, harder ionizing sources such as HOLMES should be fairly small, assuming emission with $EW_{H\alpha} < 3$ Å arises primarily from such sources. The distribution of $EW_{H\alpha}$ in M101 and NGC 5474 agrees with this, with only ~10 per cent[4] of the total H α flux in the DIG arising from pixels with $EW_{H\alpha} < 3$ Å in either galaxy. Using their criteria, the remainder of the DIG must be ionized by a mixture of sources, including photoionization.

We thus turn our attention to leakage of LyC photons from H II regions. To assess the contribution from this source, we performed an array of simulations using the spectral synthesis code Cloudy (Ver. 17.03; Ferland et al. 2017) in an attempt to reproduce the trend between $\log(Q_{10})$ and DIG $I_{H\alpha}$ displayed in Fig. 6. We created a synthetic young star cluster as our illumination source using the code Starburst99 (Ver.7.0.0; Leitherer et al. 1999; Vázquez & Leitherer 2005; Leitherer et al. 2010, 2014), with stellar mass of $10^6 \mathcal{M}_\odot$. With this illumination source, selecting an age of 2 Myr, we ran an array of CLOUDY simulations using the Φ(H) parameter option, which allows one to specify directly the incident ionizing photon flux (in photons s^{-1} cm^{-2}) on the surface of a cloud. We used a cloud with a gas density of 1 cm^{-3} as the target, and set $\log(\Phi(H)) = 2$–10 in steps of 1. We then recorded the resulting cloud's emergent $I_{H\alpha}$, excluding reflection and transmission as we are viewing these clouds in M101 and NGC 5474 from above, while the H II region flux incident on the clouds would be predominantly in the disc plane.

In Fig. 12, we overplot these model surface brightnesses on the $\log(Q_{10}) - \log(I_{H\alpha})$ relation from the left-hand panel of Fig. 6, as a red curve. We found that the shape of this curve is insensitive to the ionizing source, as, unlike line ratios, H α emission measure is merely a function of the ionization and recombination rate and hence the total incident ionizing flux, not the ionizing spectrum (Field 1975). The curve shape is also insensitive to the chosen gas density, save for densities much higher than typically found in the DIG (>100 cm^{-3}), and to the choice of filling factor and grain composition.

The match between the predicted and observed $I_{H\alpha}$ is remarkable. Above the image noise threshold, the close agreement between the predicted and observed values implies that the majority of the ionizing flux producing DIG in M101 and its companion arises from LyC leakage from H II regions. Excluding the hard ionized DIG

[4]This is an upper limit. In our images, $EW_{H\alpha}$ declines with distance from H II regions, suggesting low-$EW_{H\alpha}$ regions could be the result of geometric dilution, not necessarily a change of ionization source.

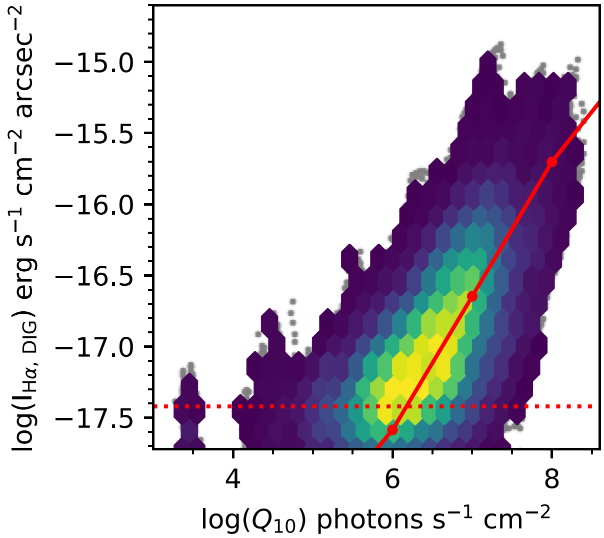

Figure 12. As the left-hand panel of Fig. 6, excluding the best-fitting relation. The red curve shows H α surface brightness predicted by a series of CLOUDY simulations, in which the incident ionizing flux on a plane-parallel cloud was set to values between $2 \leq \log(Q) \leq 10$ photons s^{-1} cm^{-2} (see the text for details).

using the criteria from Lacerda et al. (2018), this contribution would be $\gtrsim$90 per cent.

As discussed in Section 4.1, we used the measured H α luminosities of each H II region, diluted only geometrically within the disc plane, to estimate the LyC flux incident on each DIG pixel. This presumes f_{esc} = 50 per cent, and the good agreement between the Cloudy models and our data provides support that this value is approximately correct. Estimates from the literature seem to concur, albeit with a wide variability. For example, a study by Teh et al. (2023) found that H II regions with $\log(L_{H\alpha}) < 38.06$ erg s^{-1} have $f_{esc} \sim 0.56^{+0.08}_{-0.14}$ (lower for brighter populations). In the M101 Group, $\log(L_{H\alpha}) = 38.06$ erg s^{-1} is $\log(F_{H\alpha}) \sim -13.7$ erg s^{-1} cm^{-2}; only ~15 per cent of the H II regions in M101 lie above this value. In more tentative agreement, Della Bruna et al. (2021) find a value of $f_{esc} \sim 0.67^{+0.08}_{-0.12}$ among a small sample of mostly more luminous H II regions in NGC 7793. Pellegrini et al. (2012) likewise estimated a luminosity-weighted mean $f_{esc} \sim 40$ per cent in the Large and Small Magellanic Clouds.

Molecular cloud evolution models show that f_{esc} is a strong function of age, rising from nearly zero to nearly one within around 5 Myr (depending on the ionizing cluster's luminosity, the gas-phase metallicity, the star formation efficiency, and other factors; e.g. Rahner et al. 2017; Kimm et al. 2022). If so, it may not be surprising if the H II region population in a galaxy with a steady SFR over gigayear timescales has a mean f_{esc} falling roughly halfway between zero and one. This does not mean that all radiation escaping from the H II regions escapes the galaxy as a whole, of course: likely this escape is not omni-directional, and whether this escaping emission ionizes the galaxy's own ISM or leaves to ionize the IGM depends both on the directionality of the escape from the cloud and the location of the cloud within the galaxy itself (e.g. Pellegrini et al. 2012; Kim et al. 2023).

Because SFR and LyC flux are both related to $L_{H\alpha}$ by a scale factor, a loss of half of the LyC flux to leakage would reduce the $SFR_{H\alpha}$ estimated from $L_{H\alpha}$ by a factor of 2. Assuming the values of SFR_{FUV} are accurate, this agrees well with the average value of $SFR_{H\alpha}/SFR_{FUV} \sim 0.44$ we find among the H II regions. In one way, this is expected: the SFR calibration we employ was initially derived by Kennicutt (1983), who in the subsequent iterations we employ (Kennicutt 1998; Kennicutt & Evans 2012) still assumed a constant SFR over >100 Myr timescales and Case B recombination (Brocklehurst 1971) without LyC leakage, which they state provides a lower limit on the true SFR. Even so, estimating the LyC leakage fraction is not a trivial exercise, so the value we propose here, while reasonable, should be considered a fairly rough estimate.

This experiment is an alternative version of that performed by Zurita et al. (2002), Seon (2009), and most recently Belfiore et al. (2022), who used the measured H II region fluxes in their galaxies to predict the DIG surface brightness distribution. Our model differs in that we did not include attenuation of the ionizing radiation through the ISM. However, our results mirror theirs insofar as they imply a very large mean free path (>1 kpc) is required to explain the DIG surface brightness via H II region leakage alone. Seon (2009) claimed that the necessary absorption coefficient was unphysically low for reasonable models of the ISM, however Belfiore et al. (2022) explained this by suggesting it may result from DIG lying preferentially above the cold gas disc (with scale height ∼100 pc), in a region where most of the ISM is ionized (in accord with studies of DIG in edge-on galaxies, where DIG scale heights are of order 1–2 kpc; Collins & Rand 2001; Miller & Veilleux 2003; Levy et al. 2019; Rautio et al. 2022).

As M101 and NGC 5474 are both face-on, we cannot easily corroborate this explanation, but the good agreement between our simple Cloudy model comparison with our data and the results of these past studies provides further evidence that leakage of LyC photons from H II regions is sufficient to explain most of the ionizing power of the DIG here. The discrepancy between integrated Hα and FUV SFRs in the LSB regime in this group may therefore reflect the combination of a longer SFR duty cycle in that regime, leading to a more noticeable mixture of old and young massive stars, and the tendency for H II regions to lose ∼50 per cent of their LyC photons to leakage, on average. The former may be a direct consequence of the group's unique interaction history, so it is unclear how transferable this might be to other LSB environments.

5.3 Implications beyond the M101 Group

Having established that what we have defined, morphologically, as DIG represents a distinct physical environment compared to the point-like sources we identified as H II regions, we consider here a unifying physical model of the ionized gas in M101 and its companion. We do this by relating our observations to those of Hα emission in the MW.

Madsen et al. (2006) found that classical H II regions in our Galaxy (bright emission line regions immediately surrounding hot stars) show much more consistent temperatures and line ratios than DIG (everything else). DIG temperature, by contrast, appears to depend on its distance from such regions, or else it depends on the specific ionization mechanism (e.g. supernova feedback rather than photoionization). In our scenario, where DIG seems primarily ionized by LyC leakage, the gradually degrading relationship between $SFR_{H\alpha}$ and SFR_{FUV} might be illustrating similar behavior in M101 and its companion.

One obvious problem with our DIG definition is its dependence on image resolution, however. For example, even though M101 is nearby, many of its faintest H II regions, with small diameters, could blend in with what we defined as DIG, imposing a hard, resolution-dependent size cut-off on what we define as H II regions. Also, H II regions at advanced ages tend to be more diffuse and patchy than younger regions (Hannon et al. 2019), which would also blend in with DIG in unresolved imaging, yielding an age-limit on this H II region definition as well (assuming that evolved H II regions are fundamentally distinguishable from DIG, which they may not be; Rousseau-Nepton et al. 2018). More distant galaxies would suffer more from these systematic effects, and their impact on the correlations we explore here would be difficult to discern without a comparison study using higher resolution imaging of the same regions. Even so, our analysis does suffer less from such effects compared to those using integrated H α and FUV fluxes from whole galaxies, or even those using integrated fluxes over significantly larger apertures than what we use here (>100 pc).

If what we observe in the M101 Group is universal, DIG is comprised primarily of gas ionized by leakage from H II regions, and so total Hα emission should constitute an accurate estimate of the instantaneous SFR (e.g. Magaña-Serrano et al. 2020). In low-SFR environments, however, such as dwarf galaxies, LSB galaxies, and outer discs, where the classical H II region density is low (e.g. Schombert, McGaugh & Maciel 2013), the instantaneous SFR and the longer-term SFR probed by FUV emission would tend to diverge as observed, depending on the relative extent of FUV compared to Hα emission. If the IMF is invariant (as suggested, in the M101 Group, by our previous results; Watkins et al. 2017), this scenario suggests that variability in the $SFR_{H\alpha}/SFR_{FUV}$ ratio in the LSB regime is purely an artifact of the longer star formation duty cycle in that regime. If the IMF is variable, however, an idea with some observational and theoretical support (e.g. Meurer et al. 2009; Pflamm-Altenburg et al. 2009; Conroy & van Dokkum 2012; Geha et al. 2013; Li et al. 2023, and many others), the variability in that ratio must arise from a complex interaction between that IMF variability and the star-formation duty cycle. Extrapolating our methodology to other nearby galaxies may help to disentangle these competing scenarios.

6 SUMMARY

We present H α and FUV photometry of DIG and H II regions in the nearby M101 Group. We find a strong correlation between the H α surface brightness ($I_{H\alpha}$) in the DIG and the incident ionizing flux on each DIG region from its nearest ten H II regions (Q_{10}), assuming a Lyman continuum escape fraction of $f_{esc} = 0.5$. This suggests that flux leakage from H II regions is an important contributor to DIG. Likewise, we find a strong correlation between H α and FUV surface brightness in DIG regions, suggesting that field O and B stars may contribute as well.

However, integrated FUV−NUV colours of DIG regions are quite red (∼0.3) compared to H II regions (∼0.05), implying the young stellar populations embedded within the DIG are predominantly low-mass and thus likely contribute little to DIG ionization. By contrast, using a suite of Cloudy models, in which we ionize a slab of gas with a slew of ionizing photon fluxes, we reproduced the correlation between $I_{H\alpha}$ and Q_{10} very well. This suggests that most of the DIG in the M101 Group can be explained by leakage of Lyman continuum photons from H II regions, with little contribution from field OB stars or other sources. The excellent match between this predicted and observed $I_{H\alpha}$–Q_{10} relation is intriguing, as it implies the value of $f_{esc} = 0.5$ we chose is correct (in tentative agreement with past studies; e.g. Della Bruna et al. 2021; Teh et al. 2023). Also, as we did not include absorption within the ISM in our models, we find good agreement with similar analyses of other galaxies, in which the estimated mean free path of ionizing radiation in the ISM is very high (>1 kpc; Seon 2009; Belfiore et al. 2022).

We compared the SFRs derived from H α and FUV in both the DIG and H II regions. In the DIG, H α under-predicts SFR compared to FUV everywhere, with the ratio $SFR_{H\,\alpha}/SFR_{FUV}$ declining as a function of $SFR_{H\,\alpha}$. In the H II regions, which we define as all point-like sources identified within both galaxies from our Hα difference image, the ratio is flat at a value of 0.44 to the faintest regions we detect ($SFR_{H\alpha} \sim 10^{-5}\mathcal{M}_\odot$ yr^{-1}). Given this, we suspect that these point-like regions are mostly leaky, compact Strömgren spheres, while the DIG comprises a mix of faint or old H II regions and true diffuse gas.

By doing photometry within larger apertures which mix DIG, H II regions, and FUV with no H α counterpart – both using boxes with widths of ~600 pc and using azimuthal averaging – we reproduce a trend found in other galaxies, in which $SFR_{H\,\alpha}/SFR_{FUV}$ decreases with $SFR_{H\,\alpha}$ below $SFR_{H\alpha} \sim 0.003\mathcal{M}_\odot$ yr^{-1} (Lee et al. 2009, 2016; Byun et al. 2021). Diffuse FUV without a detectable H α counterpart is wide-spread throughout the M101 Group, mostly in regions with low surface brightness, which explains why including all flux in the apertures (not only H α-selected flux) results in this trend here.

The M101 Group's SFH is defined by a recent interaction between M101 and NGC 5474, resulting in a burst of star formation 300–400 Myr ago (Mihos et al. 2013, 2018; Linden & Mihos 2022). Thus, the declining SFR ratio with $SFR_{H\,\alpha}$ we find on these large scales in this group may result simply by mixing remnants from this burst (detectable as FUV emission with no H α counterpart) with on-going star formation (detectable as H II regions and the diffuse gas they ionize around them). Repeating this analysis – separating DIG from point-like, classical H II regions – in other galaxies should help discern whether or not this is unique to the M101 Group.

ACKNOWLEDGEMENTS

AEW acknowledges support from the Science and Technology Facilities Council (STFC) [grant numbers ST/S00615X/1 and ST/X001318/1]. JCM thanks the Mt Cuba Astronomical Foundation for funding support. We thank the anonymous referee for their careful reading and thoughtful comments, which helped improve the quality of the manuscript. We thank Johan Knapen, Chris Collins, and Sugata Kaviraj for many insightful discussions which helped shape the course of this work. This work made use of ASTROPY:[5] a community-developed core PYTHON package and an ecosystem of tools and resources for astronomy (Astropy Collaboration et al. 2013, 2018, 2022). This work also made use of the SCIPY (version 1.10.0) library (Virtanen et al. 2020) and the NUMPY (version 1.23.5) library (Harris et al. 2020). Figures in this paper were created using the MATPLOTLIB (version 3.6.2) library (Hunter 2007). Calculations in Section 5.2 were performed with version 17.03 of Cloudy (Ferland et al. 2017). The authors are honored to be permitted to conduct astronomical research on Iolkam Du'ag (Kitt Peak), a mountain with particular significance to the Tohono O'odham.

DATA AVAILABILITY

All *GALEX* data used in this study is available publicly through the Mikulski Archive for Space Telescopes (MAST), at the following URL: https://galex.stsci.edu/GR6/. The Burrell-Schmidt Telescope data used in this study is available on reasonable request to the authors.

[5] http://www.astropy.org

REFERENCES

Astropy Collaboration et al., 2013, A&A, 558, A33
Astropy Collaboration et al., 2018, AJ, 156, 123
Astropy Collaboration et al., 2022, ApJ, 935, 167
Battisti A. J., Calzetti D., Chary R. R., 2017, ApJ, 851, 90
Belfiore F. et al., 2022, A&A, 659, A26
Bell E. F., Kennicutt R. C., Jr, 2001, ApJ, 548, 681
Bennet P., Sand D. J., Crnojević D., Spekkens K., Karunakaran A., Zaritsky D., Mutlu-Pakdil B., 2020, ApJ, 893, L9
Berkhuijsen E. M., Mitra D., Mueller P., 2006, Astron. Nachr., 327, 82
Bigiel F., Leroy A., Walter F., Brinks E., de Blok W. J. G., Madore B., Thornley M. D., 2008, AJ, 136, 2846
Blaauw A., 1961, Bull. Astron. Inst. Netherlands, 15, 265
Blanc G. A., Heiderman A., Gebhardt K., Evans N. J. II, Adams J., 2009, ApJ, 704, 842
Boggs P. T., J. Donaldson, 1989, National Institute of Standards and Technology, Gaithersburg,
Boquien M., Burgarella D., Roehlly Y., Buat V., Ciesla L., Corre D., Inoue A. K., Salas H., 2019, A&A, 622, A103
Brocklehurst M., 1971, MNRAS, 153, 471
Burgarella D., Buat V., Iglesias-Páramo J., 2005, MNRAS, 360, 1413
Byun W. et al., 2021, ApJ, 918, 82
Chisari N. E. et al., 2018, MNRAS, 480, 3962
Collins J. A., Rand R. J., 2001, ApJ, 551, 57
Congiu E. et al., 2023, A&A, 672, A148
Conroy C., van Dokkum P. G., 2012, ApJ, 760, 71
Crocker A. F., Chandar R., Calzetti D., Holwerda B. W., Leitherer C., Popescu C., Tuffs R. J., 2015, ApJ, 808, 76
Croxall K. V., Pogge R. W., Berg D. A., Skillman E. D., Moustakas J., 2016, ApJ, 830, 4
de Mink S. E., Brott I., Cantiello M., Izzard R. G., Langer N., Sana H., 2012, in Drissen L., Robert C., St-Louis N., Moffat A. F. J., eds, Astronomical Society of the Pacific Conference Series Vol. 465, Proceedings of a Scientific Meeting in Honor of Anthony F. J. Moffat, Astronomical Society of 65the Pacific, San Francisco CA, 65
de Wit W. J., Testi L., Palla F., Zinnecker H., 2005, A&A, 437, 247
Della Bruna L. et al., 2021, A&A, 650, A103
Dettmar R. J., 1990, A&A, 232, L15
Devine D., Bally J., 1999, ApJ, 510, 197
Domgorgen H., Mathis J. S., 1994, ApJ, 428, 647
Dopita M. A., Sutherland R. S., 1995, ApJ, 455, 468
Ellis G. R. A., Waterworth M. D., Bessell M., 1962, Nature, 196, 1079
Emami N., Siana B., Weisz D. R., Johnson B. D., Ma X., El-Badry K., 2019, ApJ, 881, 71
Erroz-Ferrer S. et al., 2019, MNRAS, 484, 5009
Ferguson A. M. N., Wyse R. F. G., Gallagher J. S., III, Hunter D. A., 1996, AJ, 111, 2265
Ferland G. J. et al., 2017, RMxAA, 53, 385
Field G. B., 1975, in Balian R., Encrenaz P., Lequeux J., eds, Atomic and Molecular Physics and the Interstellar Matter; Proceedings of the Twenty-sixth Summer School of Theoretical Physics, Les Houches, France, North-Holland Publishing Co., Amsterdam. p. 467
Flores-Fajardo N., Morisset C., Stasińska G., Binette L., 2011, MNRAS, 415, 2182
French H. B., 1980, ApJ, 240, 41
Gaia Collaboration, 2022, VizieR Online Data Catalog. p. 358, https://ui.adsabs.harvard.edu/abs/2023A%26A...680A..36G/abstract
Gaia Collaboration et al., 2018, A&A, 616, A1
Garner R., Mihos J. C., Harding P., Watkins A. E., 2021, ApJ, 915, 57
Garner R., Mihos J. C., Harding P., Watkins A. E., McGaugh S. S., 2022, ApJ, 941, 182
Garner R., Mihos J. C., Harding P., Garner C. R., 2024, ApJ, 961, 217

Gaustad J. E., McCullough P. R., Rosing W., Van Buren D., 2001, PASP, 113, 1326
Gavazzi G., Zaccardo A., Sanvito G., Boselli A., Bonfanti C., 2004, A&A, 417, 499
Geha M. et al., 2013, ApJ, 771, 29
Gies D. R., 1987, ApJS, 64, 545
Gil de Paz A. et al., 2005, ApJ, 627, L29
Gil de Paz A. et al., 2007, ApJS, 173, 185
Goddard Q. E., Kennicutt R. C., Ryan-Weber E. V., 2010, MNRAS, 405, 2791
González Delgado R. M., Leitherer C., Heckman T. M., 1999, ApJS, 125, 489
Gordon K. D., Cartledge S., Clayton G. C., 2009, ApJ, 705, 1320
Haffner L. M., Reynolds R. J., Tufte S. L., 1999, ApJ, 523, 223
Haffner L. M., Reynolds R. J., Tufte S. L., Madsen G. J., Jaehnig K. P., Percival J. W., 2003, ApJS, 149, 405
Haffner L. M. et al., 2009, Rev. Mod. Phys., 81, 969
Haigh C., Chamba N., Venhola A., Peletier R., Doorenbos L., Watkins M., Wilkinson M. H. F., 2021, A&A, 645, A107
Hannon S. et al., 2019, MNRAS, 490, 4648
Harris C. R. et al., 2020, Nature, 585, 357
Hill A. S., Benjamin R. A., Haffner L. M., Gostisha M. C., Barger K. A., 2014, ApJ, 787, 106
Ho I. T. et al., 2014, MNRAS, 444, 3894
Høg E. et al., 2000, A&A, 355, L27
Hoopes C. G., Walterbos R. A. M., 2000, ApJ, 541, 597
Hoopes C. G., Walterbos R. A. M., Bothun G. D., 2001, ApJ, 559, 878
Hoyle F., Ellis G. R. A., 1963, Aust. J. Phys., 16, 1
Hunter J. D., 2007, Comput. Sci. Eng., 9, 90
Hunter D. A., Gallagher J. S., III, 1990, ApJ, 362, 480
Jing Y. P., Zhang P., Lin W. P., Gao L., Springel V., 2006, ApJ, 640, L119
Keel W. C. et al., 2012, MNRAS, 420, 878
Kennicutt R. C., Jr, 1983, ApJ, 272, 54
Kennicutt R. C., Jr, 1998, ARA&A, 36, 189
Kennicutt R. C., Evans N. J., 2012, ARA&A, 50, 531
Kennicutt R. C., Jr, Edgar B. K., Hodge P. W., 1989, ApJ, 337, 761
Kennicutt R. C., Jr, Lee J. C., Funes J. G., J. S., Sakai S., Akiyama S., 2008, ApJS, 178, 247
Kim K. J. et al., 2023, ApJ, 955, L17
Kimm T., Bieri R., Geen S., Rosdahl J., Blaizot J., Michel-Dansac L., Garel T., 2022, ApJS, 259, 21
Kotulla R., Fritze U., Weilbacher P., Anders P., 2009, MNRAS, 396, 462
Lacerda E. A. D. et al., 2018, MNRAS, 474, 3727
Lamb J. B., Oey M. S., Werk J. K., Ingleby L. D., 2010, ApJ, 725, 1886
Lamb J. B., Oey M. S., Graus A. S., Adams F. C., Segura-Cox D. M., 2013, ApJ, 763, 101
Lazarian A., Eyink G. L., Jafari A., Kowal G., Li H., Xu S., Vishniac E. T., 2020, Physics of Plasmas, 27, 012305
Lee J. C. et al., 2009, ApJ, 706, 599
Lee J. C., Veilleux S., McDonald M., Hilbert B., 2016, ApJ, 817, 177
Lehnert M. D., Heckman T. M., Weaver K. A., 1999, ApJ, 523, 575
Leitherer C. et al., 1999, ApJS, 123, 3
Leitherer C., Ortiz Otálvaro P. A., Bresolin F., Kudritzki R.-P., Lo Faro B., Pauldrach A. W. A., Pettini M., Rix S. A., 2010, ApJS, 189, 309
Leitherer C., Ekström S., Meynet G., Schaerer D., Agienko K. B., Levesque E. M., 2014, ApJS, 212, 14
Leroy A. K., Walter F., Brinks E., Bigiel F., de Blok W. J. G., Madore B., Thornley M. D., 2008, AJ, 136, 2782
Levy R. C. et al., 2019, ApJ, 882, 84
Li J., Liu C., Zhang Z.-Y., Tian H., Fu X., Li J., Yan Z.-Q., 2023, Nature, 613, 460
Linden S. T., Mihos J. C., 2022, ApJ, 933, L33
Madsen G. J., Reynolds R. J., Haffner L. M., 2006, ApJ, 652, 401
Magaña-Serrano M. A., Hidalgo-Gámez A. M., Vega-Acevedo I., Castañeda H. O., 2020, RMxAA, 56, 39
Marino R. A. et al., 2013, A&A, 559, A114
Martin D. C. et al., 2005, ApJ, 619, L1
Matheson T. et al., 2012, ApJ, 754, 19
Mathis J. S., 2000, ApJ, 544, 347
McKee C. F., Ostriker J. P., 1977, ApJ, 218, 148
Meurer G. R. et al., 2009, ApJ, 695, 765
Mihos J. C., Harding P., Spengler C. E., Rudick C. S., Feldmeier J. J., 2013, ApJ, 762, 82
Mihos J. C., Durrell P. R., Feldmeier J. J., Harding P., Watkins A. E., 2018, ApJ, 862, 99
Miller S. T., Veilleux S., 2003, ApJS, 148, 383
Morrissey P. et al., 2007, ApJS, 173, 682
Moustakas J., Kennicutt R. C., Jr, 2006, ApJS, 164, 81
Muñoz-Mateos J. C. et al., 2015, ApJS, 219, 3
Müller O., Scalera R., Binggeli B., Jerjen H., 2017, A&A, 602, A119
Negroponte J., White S. D. M., 1983, MNRAS, 205, 1009
Noll S., Burgarella D., Giovannoli E., Buat V., Marcillac D., Muñoz-Mateos J. C., 2009, A&A, 507, 1793
Oey M. S., King N. L., Parker J. W., 2004, AJ, 127, 1632
Oey M. S., Lamb J. B., Kushner C. T., Pellegrini E. W., Graus A. S., 2013, ApJ, 768, 66
Oey M. S. et al., 2018, ApJ, 867, L8
Osterbrock D. E., Ferland G. J., 2006, Astrophysics of Gaseous Nebulae and Active Galactic Nuclei, University Science Books, Sausalito, CA
Otte B., Reynolds R. J., Gallagher J. S., III, Ferguson A. M. N., 2001, ApJ, 560, 207
Pellegrini E. W., Oey M. S., Winkler P. F., Points S. D., Smith R. C., Jaskot A. E., Zastrow J., 2012, ApJ, 755, 40
Pflamm-Altenburg J., Weidner C., Kroupa P., 2009, MNRAS, 395, 394
Rahner D., Pellegrini E. W., Glover S. C. O., Klessen R. S., 2017, MNRAS, 470, 4453
Rand R. J., 1998, ApJ, 501, 137
Rand R. J., Kulkarni S. R., Hester J. J., 1990, ApJ, 352, L1
Rautio R. P. V., Watkins A. E., Comerón S., Salo H., Díaz-García S., Janz J., 2022, A&A, 659, A153
Raymond J. C., 1992, ApJ, 384, 502
Reber G., Ellis G. R., 1956, J. Geophys. Res., 61, 1
Relaño M., Kennicutt R. C., Jr, Eldridge J. J., Lee J. C., Verley S., 2012, MNRAS, 423, 2933
Renzo M. et al., 2019, A&A, 624, A66
Reynolds R. J., 1990, ApJ, 349, L17
Reynolds R. J., Roesler F. L., Scherb F., 1973, ApJ, 179, 651
Rousseau-Nepton L., Robert C., Martin R. P., Drissen L., Martin T., 2018, MNRAS, 477, 4152
Salembier P., Oliveras A., Garrido L., 1998, IEEE Trans. Image Proc., 7, 555
Schlafly E. F., Finkbeiner D. P., 2011, ApJ, 737, 103
Schombert J., McGaugh S., Maciel T., 2013, AJ, 146, 41
Seon K.-I., 2009, ApJ, 703, 1159
Simpson J. P., Colgan S. W. J., Cotera A. S., Erickson E. F., Hollenbach D. J., Kaufman M. J., Rubin R. H., 2007, ApJ, 670, 1115
Sullivan M., Treyer M. A., Ellis R. S., Mobasher B., 2004, MNRAS, 350, 21
Teeninga P., Moschini U., Trager S. C., Wilkinson M. H. F., 2013, in 11th International Conference 'Pattern Recognition and Image Analysis', IPSI RAS, Samara, Russia. p. 746
Teeninga P., Moschini U., Trager S. C., Wilkinson M. H. F., 2016, Mathematical Morphology – Theory and Applications, 1, 100
Teh J. W. et al., 2023, MNRAS, 524, 1191
Thilker D. A., Braun R., Walterbos R. A. M., 2000, AJ, 120, 3070
Thilker D. A. et al., 2005, ApJ, 619, L79
Thilker D. A. et al., 2007, ApJS, 173, 538
van Daalen M. P., Schaye J., Booth C. M., Dalla Vecchia C., 2011, MNRAS, 415, 3649
Vargas-Salazar I., Oey M. S., Barnes J. R., Chen X., Castro N., Kratter K. M., Faerber T. A., 2020, ApJ, 903, 42
Vázquez G. A., Leitherer C., 2005, ApJ, 621, 695
Virtanen P. et al., 2020, Nat. Methods, 17, 261

Walter F., Brinks E., de Blok W. J. G., Bigiel F., Kennicutt R. C., Jr, Thornley M. D., Leroy A., 2008, AJ, 136, 2563
Walterbos R. A. M., Braun R., 1992, A&AS, 92, 625
Watkins A. E., Mihos J. C., Harding P., 2017, ApJ, 851, 51
Watkins A. E., Mihos J. C., Bershady M., Harding P., 2018, ApJ, 858, L16
Weaver T. A., Zimmerman G.B., Woosley S. E., 1978, Astrophysical Journal,225,1021
Weisz D. R. et al., 2012, ApJ, 744, 44
Windhorst R. A. et al., 2023, AJ, 165, 13
Wood K., Mathis J. S., 2004, MNRAS, 353, 1126
Wood K., Haffner L. M., Reynolds R. J., Mathis J. S., Madsen G., 2005, ApJ, 633, 295
Zhang K. et al., 2017, MNRAS, 466, 3217
Zurita A., Beckman J. E., Rozas M., Ryder S., 2002, A&A, 386, 801

This paper has been typeset from a TEX/LATEX file prepared by the author.